HYDROLOGICAL PROCESSES
Hydrol. Process. **30**, 4036–4058 (2016)
Published online 30 August 2016 in Wiley Online Library
(wileyonlinelibrary.com) DOI: 10.1002/hyp.10971

Modelling the hydrological response of debris-free and debris-covered glaciers to present climatic conditions in the semiarid Andes of central Chile

A. Ayala,[1]* F. Pellicciotti,[1,2] S. MacDonell,[3] J. McPhee,[4,5] S. Vivero,[3] C. Campos[3] and P. Egli[1]

[1] *Institute of Environmental Engineering, ETH Zurich, Stefano-Franscini-Platz 5, 8093 Zurich, Switzerland*
[2] *Department of Geography, Faculty of Engineering and Environment, Northumbria University, Newcastle upon Tyne, UK*
[3] *Centro de Estudios Avanzados en Zonas Áridas (CEAZA), Universidad de La Serena, Raúl Bitrán 1305, La Serena, Chile*
[4] *Department of Civil Engineering, Faculty of Physical and Mathematical Sciences, University of Chile, Av. Blanco Encalada 2002, Santiago, Chile*
[5] *Advanced Mining Technology Centre (AMTC), Faculty of Physical and Mathematical Sciences, University of Chile, Av. Tupper 2007, Santiago, Chile*

Abstract:

We apply the process-based, distributed TOPKAPI-ETH glacio-hydrological model to a glacierized catchment (19% glacierized) in the semiarid Andes of central Chile. The semiarid Andes provides vital freshwater resources to valleys in Chile and Argentina, but only few glacio-hydrological modelling studies have been conducted, and its dominant hydrological processes remain poorly understood. The catchment contains two debris-free glaciers reaching down to 3900 m asl (Bello and Yeso glaciers) and one debris-covered avalanche-fed glacier reaching to 3200 m asl (Piramide Glacier). Our main objective is to compare the mass balance and runoff contributions of both glacier types under current climatic conditions. We use a unique dataset of field measurements collected over two ablation seasons combined with the distributed TOPKAPI-ETH model that includes physically oriented parameterizations of snow and ice ablation, gravitational distribution of snow, snow albedo evolution and the ablation of debris-covered ice. Model outputs indicate that while the mass balance of Bello and Yeso glaciers is mostly explained by temperature gradients, the Piramide Glacier mass balance is governed by debris thickness and avalanches and has a clear non-linear profile with elevation as a result. Despite the thermal insulation effect of the debris cover, the mass balance and contribution to runoff from debris-free and debris-covered glaciers are similar in magnitude, mainly because of elevation differences. However, runoff contributions are distinct in time and seasonality with ice melt starting approximately four weeks earlier from the debris-covered glacier, what is of relevance for water resources management. At the catchment scale, snowmelt is the dominant contributor to runoff during both years. However, during the driest year of our simulations, ice melt contributes $42 \pm 8\%$ and $67 \pm 6\%$ of the annual and summer runoff, respectively. Sensitivity analyses show that runoff is most sensitive to temperature and precipitation gradients, melt factors and debris cover thickness. Copyright © 2016 John Wiley & Sons, Ltd.

KEY WORDS glacio-hydrological models; debris-covered glaciers; semiarid Andes; TOPKAPI-ETH

Received 30 November 2015; Accepted 20 July 2016

INTRODUCTION

The cryosphere of the Andes Cordillera significantly contributes freshwater to streams flowing into the semiarid regions of central Chile and Argentina (~33.5°S). Accurate quantification of snow and ice melt is of critical importance for water managers in this region because of a heightened demand for water (Meza *et al*., 2015) exacerbated by a recent prolonged drought period (Boisier *et al*., 2015). Hydrological studies that model melt from glaciers and seasonal snow cover remain, however, scarce (Favier *et al*., 2009; Ragettli and Pellicciotti, 2012; Ragettli *et al*., 2013a) or outdated (Peña and Nazarala, 1987), and have not explicitly considered the contribution from debris-covered and rock glaciers, which are common features in the region (Azócar and Brenning, 2010; Bodin *et al*., 2010).

Excluding local efforts from the Chilean Water Authority (*Dirección General de Aguas*, DGA), which have investigated high-elevation water resources with more statistical approaches (Peña *et al*., 1985), the first physically oriented modelling study to quantify runoff sources in this region was performed by Peña and Nazarala (1987). They used a semi-distributed empirical snowmelt-runoff model to simulate the hydrology of the Maipo river basin (4837 km^2, 8% glacierized) to the east of the Chilean capital city, Santiago. Peña and Nazarala (1987) calculated that glacier melt, that is melt from the ice and the snow cover over the glacier, represented up

*Correspondence to: Alvaro Ayala, Institute of Environmental Engineering, ETH Zurich, Stefano-Franscini-Platz 3, HIF CO 46.5, CH-8093 Zurich, Switzerland.
E-mail: ayala@ifu.baug.ethz.ch

to 67% of the total runoff at the outlet of the catchment (800 m asl) during one of the driest summers on the hydro-meteorological record (1968/69). More than 25 years later, the estimates of Peña and Nazarala (1987) are still largely cited by scientists, private companies, NGOs and stake-holders (e.g. Larraín, 2007; Bown *et al*., 2008; Le Quesne *et al*., 2009; Ohlanders *et al*., 2013). There is a real need for updated glacio-hydrological studies because of changing climate patterns (Carrasco *et al*., 2005, 2008), new understanding of the main drivers of changes at high elevations and a growing demand for water resources (Meza *et al*., 2013). A couple of recent studies have shed light on the hydrology of high-elevation glacierized catchments of this region (Favier *et al*., 2009; Ragettli and Pellicciotti, 2012; Ragettli *et al*., 2013a), but their dynamics remain poorly understood, key components of the cryosphere are still neglected and studies have been confined to few well monitored catchments (Pellicciotti *et al*., 2014).

Ragettli and Pellicciotti (2012) used the glacio-hydrological model TOPKAPI-ETH to simulate the hydrology of the Juncal Norte River catchment (241 km^2, 14% glacierized) during two hydrological years (2005–2006 and 2008–2009), based on detailed hydro-glaciological measurements. They found that ice melt amounted to approximately 47% of total contributions to runoff at the catchment scale (outlet at 2233 m asl) in the 2005 late ablation season (February–April). In a following study, Ragettli *et al*. (2013a) compared these simulations to those of a simpler, conceptual and semi-distributed model lacking glacier representation and a snow gravitational distribution algorithm (Water Evaluation and Planning) (Yates *et al*., 2005). They found that while the conceptual model can be calibrated to reproduce present-day streamflow with the same degree of accuracy as the more physically oriented one, their future projections of runoff diverge significantly, and the inclusion of the main cryospheric processes is needed for more reliable estimates of future runoff. Ohlanders *et al*. (2013) estimated the water balance of the Juncal Norte River catchment using measurements of stable isotopes and found that for the unusually dry year of 2011/2012 ice melt amounted to 50–90% of the total annual streamflow at the catchment outlet.

Most cryospheric studies in the semiarid Chilean Andes have looked at large-scale snow (Masiokas *et al*., 2006, 2010; Carrasco *et al*., 2008), mass balance (Mernild *et al*., 2015) and hydro-meteorological patterns (Rubio-Álvarez and McPhee, 2010; Cortés *et al*., 2011; Demaria *et al*., 2013) or at single, specific processes, such as energy balance studies (Brock *et al*., 2007; Pellicciotti *et al*., 2008; MacDonell *et al*., 2013a), wind snow redistribution (Gascoin *et al*., 2013) or radiation fluxes over glacier surfaces (MacDonell *et al*., 2013b; Lhermitte *et al*., 2014). Most large-scale studies are based on gridded data sets or remotely sensed data (Favier *et al*., 2009; Mernild *et al*., 2015; Cornwell *et al*., 2016), and the detailed process-based studies are mostly observational (Gascoin *et al*., 2011; Sinclair and MacDonell, 2015) or use point scale models (Pellicciotti *et al*., 2008), so that a clear gap emerges between the two scales and type of studies, with distributed, physically oriented, glacio-hydrological modelling studies almost entirely lacking in the region (Pellicciotti *et al*., 2014).

Additionally, rock and debris-covered glaciers are often excluded from hydrological analyses in the region. These features have been documented in mapping and classification studies (Bodin *et al*., 2010; Nicholson *et al*., 2010; Janke *et al*., 2015) but rarely modelled or included in glacio-hydrological studies. For example, Azócar and Brenning (2010) estimated that the water equivalent of ice stored in rock glaciers in the Chilean Andes between 27° and 33°S is 2.37 km^3 with average thinning rates in the order of 0.6–0.7 mm yr^{-1}. In another study, using GPR observations in Tapado Glacier foreland, Pourrier *et al*. (2014) showed that the internal structure of rock glaciers can be highly heterogeneous with the presence of massive ice lenses. In other regions of the world, it has been shown that despite the assumed insulation effect of the debris, debris-covered glaciers might lose as much mass as debris-free glaciers (Gardelle *et al*., 2012, 2013; Kääb *et al*., 2012), mainly because of their usually lower elevation (Fujita and Sakai, 2014; Ragettli *et al*., 2015), presence of ice cliffs (Buri *et al*., 2015; Steiner *et al*., 2015) and supraglacial ponds (Sakai *et al*., 2000; Miles *et al*., 2016). Some of that evidence has been provided by large-scale studies based on remote sensing and is still controversial (e.g. Ragettli *et al*., 2016). Available observations suggest, however, that the mass balance of debris-covered glaciers is considerably different to the one of debris-free glaciers, with highly heterogeneous surface lowering (Immerzeel *et al*., 2014; Kraaijenbrink *et al*., 2016; Ragettli *et al*., 2016) and non-linear mass balance gradients (Nuimura *et al*., 2012; Pellicciotti *et al*., 2015). To our knowledge, no study has supported this evidence with results from a physically oriented model that explicitly incorporates the processes that are believed to be dominant on debris-covered glaciers.

In this paper, we build on the work of Ragettli and Pellicciotti (2012) and Ragettli *et al*. (2013a) to study the hydrological contribution of debris-covered and debris-free glaciers. Our main aims are to: (1) compare the mass balance and hydrological contribution of these two glacier types and (2) quantify the magnitude and timing of the contribution of snow and ice melt to total runoff at the catchment scale.

STUDY CATCHMENT

The Río del Yeso catchment is located in the semiarid Andes of central Chile, 70 km east of Santiago (Figure 1). The catchment has an area of 62 km^2 (19% glacierized), a mean elevation of 4007 m above sea level (asl) and it provides freshwater resources to El Yeso reservoir, which is used to manage the drinking water supply for Santiago. In this study, we focus on the three major glaciers of the catchment: Bello, Yeso and Piramide (Table I).

Despite their key location, very little research has been conducted at Bello and Yeso glaciers. To our knowledge, the only available literature comes from DGA technical reports and inventories, which are mostly descriptive (Marangunic, 1979). Bello Glacier has a south-east aspect and a southward flowing tongue, partially debris-covered at its terminus. Yeso Glacier is located next to Bello Glacier, east of a ridge descending from Bello peak (5230 m asl). It has a south-west aspect, and its tongue descends in a south-west direction. Both glaciers contribute to the Yeso River, which extends to the south for approximately 8 km before reaching the outlet defined for this study.

Piramide Glacier is a debris-covered glacier located in the neighbouring valley to the east of Yeso River. The glacier has no classically shaped accumulation area and is mainly fed by avalanches generated from the steep slopes surrounding its upper area. The glacier extends southward for about 6 km before reaching its terminus, about 2 km away from the Río del Yeso catchment outlet. The glacier is stagnant with advance velocities close to zero, a fact that can be corroborated by the absence of ridges and furrows, which are typically found on active debris-covered glaciers. Ferrando (2012) suggests that its chaotic surface topography is a product of differential ablation. Piramide Glacier has experienced a small area loss

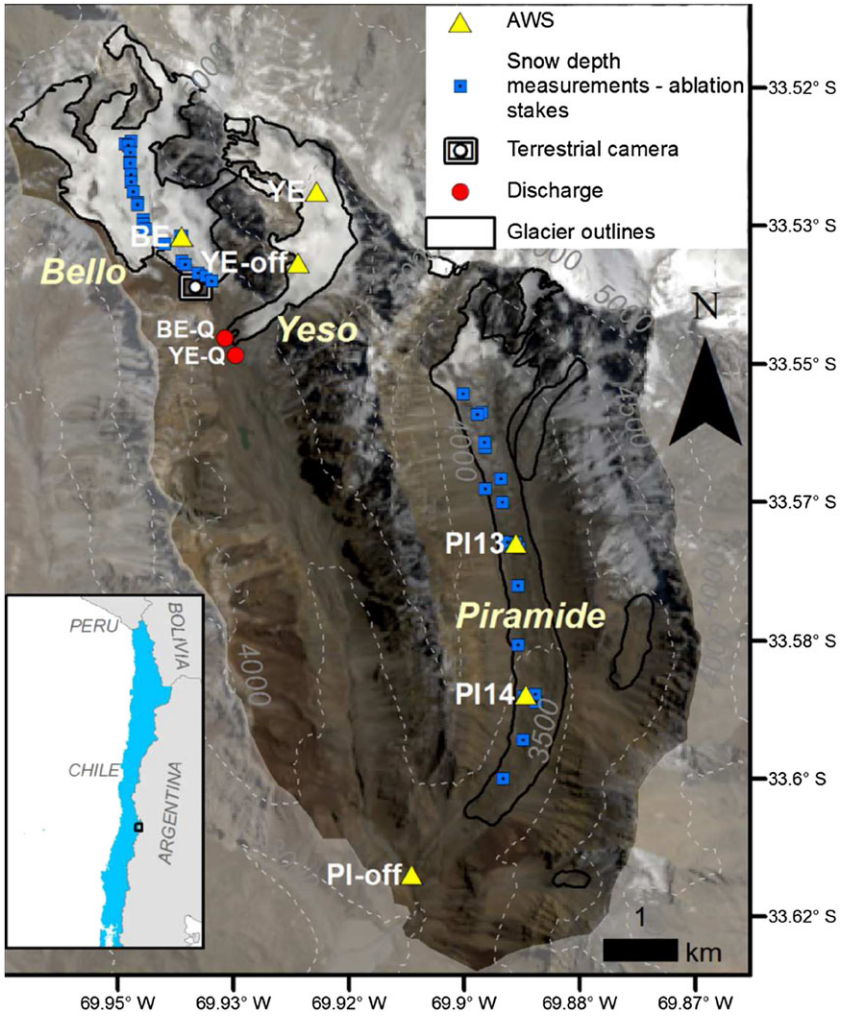

Figure 1. Location of Río del Yeso catchment in the semiarid Andes of central Chile (2972–5476 m asl). We show the location of AWSs (BE, YE, YE-off, PI13, PI14 and PI-off), the terrestrial camera, the manual measurements of streamflow (BE-Q and YE-Q) and snow depth and ablation stakes (blue squares). Background image corresponds to a true colour Landsat 8 retrieved on 19 February 2014

Table I. Main characteristics of Bello, Yeso and Piramide glaciers.

Glacier	Area [km^2]	Percentage of debris covered area [%]	Elevation range [m asl]	Mean elevation [m asl]	Glacier length [km]
Bello	4.1	2.9	3989–4925	4430	3.9
Yeso	2.2	4.1	3842–5181	4444	3.7
Piramide	4.4	100	3230–4593	3670	7.5

compared to other glaciers in this region (Janke *et al*., 2015), which is typical of debris-covered glaciers, which do not recede but rather thin or downwaste. According to Janke *et al*. (2015), the glacier has not yet reached a sufficient debris cover thickness to enable the thermal insulation of the ice body.

DATA DESCRIPTION

Hydro-meteorological data

An automatic weather station (AWS) was installed on each of the three glaciers (Figure 1 and Table II). Because of logistical constraints, for example sites with a difficult access, or locations too close to potentially dangerous slopes during winter months, the AWSs were installed at different times and some were moved during the course of the study. Another AWS was located off-glacier on the slopes surrounding Yeso and Piramide glaciers. This station was positioned near the ablation tongue of Yeso Glacier in 2013–2014 and moved to a location next to Piramide Glacier in 2014–2015. All AWSs recorded data every hour, with the exception of the AWS on Piramide Glacier that recorded data every 10 min. For this study all data were aggregated to hourly averages. A summary of the AWS locations, instruments and periods of functioning is shown in Figure 1 and Table II.

Table II. Summary of AWSs.

AWS name	Location	Coordinates (E,N) [UTM 19S]	Elevation [m asl]	Time periods	AWS	Measured variable (sensor)
BE	Bello Glacier	412744 6289113	4134	1.- 14 November 2013 to 15 April 2014 2.- 1 October 2014 to end of study period There is a data gap between 20 January and 6 February 2013 because of a problem with the battery supply.	1	Wind speed and direction (Young 05103-5) Incoming and outgoing shortwave and longwave radiation (Kipp & Zonen CNR4) Air temperature and relative humidity (Young 41382)
YE	Yeso Glacier	414554 6289714	4428	1.- 15 November 2013 to 15 April 2014 2.- 5 November 2014 to end of study period There is a data gap between 27 December 2014 and 24 February 2015, as the AWS fell into a crevasse and the battery was lost.	2	
PI13	Piramide Glacier	417222 6285012	3655	1.- 6 November 2013 to 15 April 2014	3	
PI14	Piramide Glacier	417353 6282990	3494	1.- 15 April 2014 to end of study period		
YE-off	Next to Yeso Glacier	414304 6288762	4300	1.- 15 November 2013 to 5 November 2014	4	Wind speed and direction (Vaisala WM30) Incoming and outgoing shortwave and longwave radiation (Kipp & Zonen CNR2) Air temperature and relative humidity (HMP110)
PI-off	Next to Piramide Glacier	415828 6280577	3022	1.- 5 November 2014 to end of study period		

Table III. Weather stations from the DGA network used in this study.

Name	Coordinates (Lat,Lon)	Elevation [m asl]
Embalse El Yeso (Base station for precipitation)	33.677° S, 70.089° W	2475
Laguna Negra (Base station for air temperature)	33.666° S 70.108° W	2780
Aguas Panimávida	33.806° S 70.070° W	2237

In addition to the AWSs data, we used data from the DGA meteorological network in the lower valleys to estimate off-glacier gradients of precipitation and air temperature (Table III). In order to derive cloud cover transmittance, we used the daily incident radiation ($1° \times 1°$ gridded product) from the 'Climatology Resource for Agroclimatology' project in the NASA Prediction Worldwide Energy Resource 'POWER' (http://power.larc.nasa.gov/). Finally, discharge was manually measured using salt dilution gauging at the outlet of Bello and Yeso glaciers during the ablation season (Figure 1).

Glaciological measurements

Measurements of snow depth and surface lowering were performed at Bello and Piramide glaciers in 2013 and 2014 (Figure 1). On Bello Glacier, nine ablation stakes were installed on 16 January 2014 along the glacier centerline. On Piramide Glacier, nine ablation stakes were first installed on snow on 6 November 2013 and replaced by a network installed into debris and ice once the snowpack disappeared on 29 January 2014. This second network was maintained for the rest of the study period. Snow depth measurements were performed at the end of the accumulation season on 5 November 2013 (Piramide Glacier) and on 1 October 2014 (Piramide and Bello glaciers). The location of these measurements was chosen to cover the maximum range of elevation along the centre flow line of each glacier. At each point, several snow depth measurements were performed and averaged.

Two snowpits were dug next to the AWS on Piramide Glacier to measure snow density and calculate snow water equivalent. The first snowpit was dug on 5 November 2013 (2.20-m depth, $520\,kg\,m^{-3}$ mean density), and the second on 1 October 2014 (0.7-m depth, $280\,kg\,m^{-3}$ mean density). One snowpit was dug next to the AWS on Bello Glacier on 1 October 2014 (1.7-m depth, $310\,kg\,m^{-3}$ mean density). Finally, debris cover thickness was manually measured at each ablation stake on 29 January 2014 on Piramide Glacier. These data were extended using seven additional measurements performed during 2012 (Comitato-Ev-K2-CNR, 2012).

Terrestrial photos

A time-lapse camera (Harbortronics system) was installed in front of Bello Glacier on 27 February 2014 to take daily photos of the lower section of the glacier (Figure 1). The time-lapse system included a Canon EOS Rebel T3 camera with a resolution of 12.2 MP and a focal length of 18 mm and was programmed to take photos at 13 h (Chilean summer time). We obtained a total of 48 valid photos in the period 27 February 2014 to 15 April 2014 and 114 valid photos in the period 23 October 2014 to 1 April 2015. The extension of the monitored area is $0.84\,km^2$, which corresponds to 20.5% of the total glacier surface of Bello Glacier. The daily photos were used to calculate distributed maps of surface albedo and to derive snow-covered areas (Section Reconstruction of Albedo from Terrestrial Photos).

Remote sensing products

The topography of the catchment was obtained from a Digital Elevation Model (DEM) of 30-m resolution, acquired on February 2000, extracted from the Shuttle Radar Topographic Mission. Additionally, we used a LANDSAT 8 satellite thermal image of 60-m resolution retrieved on 22 February 2015 to derive surface temperature of debris-covered areas. Finally, glacier outlines were extracted from the Chilean National glacier inventory (DGA, 2010).

THE TOPKAPI-ETH MODEL

Model description

The TOPKAPI-ETH model is a fully distributed process-based hydrological model, which was first developed by Ciarapica and Todini (2002) and Liu and Todini (2002) as a rainfall–runoff model. The main characteristic of the original model is the use of the kinematic approximation to route subsurface, overland and channel flow. Further developments have provided a set of new modules that make the model suitable for water budget analyses of high-elevation areas dominated by cryospheric processes (Finger *et al.*, 2011; Ragettli and Pellicciotti, 2012; Ragettli *et al.*, 2013a, b, 2015; Fatichi *et al.*, 2015). These modules include snow and ice melt (Pellicciotti *et al.*, 2005), melt of debris-covered ice (Carenzo *et al.*, 2015), a parameterisation of glacier geometry changes implicitly accounting for glacier flow (Huss *et al.*, 2010), snow albedo evolution (Brock *et al.*, 2000), redistribution of snow by avalanching (Bernhardt and Schulz, 2010) and melt water routing (Hock and Noetzli, 1997).

Melt from snow and bare-ice is computed in each grid cell using the Enhanced Temperature-Index (ETI) model

(Pellicciotti *et al.*, 2005):

$$M = \begin{cases} SRF \cdot I \cdot (1-\alpha) + TF \cdot T & T > T_T \\ 0 & T \leq T_T \end{cases}, \quad (1)$$

where M [mm h^{-1}] is hourly melt; SRF [m^2 mm W^{-2} h^{-1}] and TF [mm h^{-1} °C^{-1}] are shortwave radiation and temperature factors, respectively; I [W m^{-2}] is incoming shortwave radiation; α [—] is surface albedo; T [°C] is air temperature and T_T [°C] is an air temperature threshold for the onset of melt.

TOPKAPI-ETH computes melt under debris using a modification of the ETI model, which is referred to as D-ETI (Ragettli *et al.*, 2015; Carenzo *et al.*, 2015). In this approach the coefficients SRF and TF are parameterized as a function of debris thickness. A lag parameter, which is also a function of debris thickness, is introduced to represent the time needed for the energy transfer through the debris layer. The resulting set of equations is:

$$M = \begin{cases} SRF_d \cdot I(t-lag) \cdot (1-\alpha) + TF_d \cdot T(t-lag) & T > T_T \\ 0 & T \geq T_T \end{cases} \quad (2)$$

$$SRF_d = SRF_{d1} \cdot e^{-SRF_{d2} \cdot d} \quad (3)$$

$$TF_d = TF_{d1} \cdot d^{-TF_{d2}} \quad (4)$$

$$lag = lag_{d1} \cdot d - lag_{d2}, \quad (5)$$

where d [m] is debris thickness and SRF_{d1} [mm m^2 h^{-1} W^{-1}], SRF_{d2} [m^{-1}], TF_{d1} [mm h^{-1} °C^{-1}], TF_{d2} [—], lag_{d1} [h m^{-1}] and lag_{d2} [h] are parameters that were calibrated against the results of an energy balance model as a reference.

The evolution of snow albedo is calculated using the approach by Brock *et al.* (2000):

$$\alpha = \alpha_{max} - r_d \cdot \log_{10} T_{acc}, \quad (6)$$

where a_{max} [—] is the albedo of fresh snow, r_d [—] is a decay rate and T_{acc} [°C] is the accumulated daily positive maximum air temperature.

Snow gravitational redistribution is implemented using the SnowSlide model of Bernhardt and Schulz (2010), in which snow available for transport corresponds to the difference between the grid cell snow holding depth (S_{hd} [m]) and the current snow depth. The value of S_{hd} is calculated as a function of the slope angle:

$$S_{hd} = SGR_C \cdot e^{SGR_a \cdot SLP}, \quad (7)$$

where SGR_C and SGR_a are empirical parameters and SLP is the grid slope.

Snow is transferred to the lower neighbouring cells and is portioned based on the vertical distance between neighbouring and initial grid elements. The scheme allows for divergent and convergent flow and is strictly mass conserving. TOPKAPI-ETH simulates discharge from glaciers using two linear reservoirs that represent the storage of meltwater within the snowpack (k_{snow} [h]) and ice (k_{ice} [h]) (Hock and Noetzli, 1997). The long-term evolution of glacier geometry in response to climate forcing is also included in the model through a conceptual parameterization of ice flow dynamics (Huss *et al.*, 2010; Ragettli, 2014). However, the time scale of these changes is typically in the order of several years or decades, depending on glacier scale. Because of the short time span of our simulations, the ice flow module was switched off, as no significant geometry changes were expected to take place over the two years of analysis.

Forcing variables

TOPKAPI-ETH requires hourly time series of air temperature, precipitation, clear-sky incoming shortwave radiation and daily cloud transmittance factors. Air temperature and precipitation time series from stations of the DGA meteorological network were distributed over the catchment. Air temperature was distributed using monthly mean lapse rates (T_{grad}) (Table IV). To represent the temperature variations induced by the glacier boundary layer (Greuell and Böhm, 1998; Brock *et al.*, 2010), we used two parameters to decrease air temperature on debris-free glaciers ($Tmod$) and increase it on debris-covered glaciers ($Tmod_{debris}$):

$$T(z) = \begin{cases} T(z_0) + T_{grad} \cdot (z - z_0) - Tmod & Debris-free\ cell \\ T(z_0) + T_{grad} \cdot (z - z_0) + Tmod_{debris} & Debris-covered\ cell, \end{cases} \quad (8)$$

where z is the elevation of each grid cell and z_0 is the elevation of the base station. We distributed precipitation using logarithmic altitudinal gradients:

$$P(z) = \left[P_{grad\_C1} \cdot \ln(z) + P_{grad\_C2}\right] \cdot P(z_0), \quad (9)$$

where $P(z)$ [mm] is precipitation at elevation z [m asl], $P(z_0)$ [mm] is precipitation recorded at the base station and P_{grad_C1} and P_{grad_C2} are calibrated parameters.

Clear-sky incoming shortwave radiation for each grid cell is calculated by TOPKAPI-ETH following the approach described in Pellicciotti *et al.* (2011). Finally,

Table IV. TOPKAPI-ETH calibrated parameters. The most sensitive parameters are shown in bold for them and a plausible range for them is given in parentheses. The plausible range is defined by the values that produce variations of ±5% in the total annual runoff of year 2014–2015.

Name	Description	Calibrated value (plausible range)	Units	Sensitivity of total annual runoff to parameter variations	Units
Air temperature distribution (*Step 1*)					
Tgrad	Monthly average temperature gradients	Jan = −7.06 (−6.8 – −7.3) Feb = −6.44 (−6.2 – −6.7) Mar = −5.94 (−5.7 – −6.2) Apr = −5.56 (−5.4 – −5.8) May = −5.30 (−5.1 – −5.5) Jun = −5.16 (5.0 – −5.4) Jul = −5.14 (−5.0 – −5.3) Aug = −5.24 (−5.1 – −5.4) Sep = −5.46 (−5.3 – −5.7) Oct = −5.80 (−5.6 – −6.0) Nov = −6.26 (−6.0 – −6.5) Dec = −6.84 (−6.6 – −7.1)	°C/km	**−13.8**	mm $\%^{-1}$
Tmod	Temperature decrease over snow and bare ice	1	°C	−0.2	mm $\%^{-1}$
$Tmod_{debris}$	Temperature increase over glacier debris	0.3	°C	0.1	mm $\%^{-1}$
Snow and ice melt (*Step 2*)					
SRF	Parameters of ETI melt model	0.0048 (0.0041 – 0.0055)	mm m^2 h^{-1} W^{-2}	**3.5**	mm $\%^{-1}$
TF		0.1049	mm h^{-1} °C	0.4	mm $\%^{-1}$
$\boldsymbol{T_T}$		−1 (−3.5 – 0.6)	°C	**−22.8**	mm $°C^{-1}$
TF_{d1}	Parameters of D-ETI	0.0170		0.8	mm $\%^{-1}$
TF_{d2}	melt model	0.4043		0.8	mm $\%^{-1}$
SRF_{d1}		0.0114		0.8	mm $\%^{-1}$
SRF_{d2}		44.2		−0.9	mm $\%^{-1}$
lag_1		36			
lag_2		1			
$\boldsymbol{\alpha_{max}}$	Albedo of fresh snow	0.83 (0.72 – 0.91)		**−4.6**	mm $\%^{-1}$
r_d	Decay of snow albedo	0.102		0.9	mm $\%^{-1}$
Precipitation distribution (*Step 3*)					
***Pgrad* 2013 - 14**	Logarithmic coefficients for precipitation gradient	−5	—		
***Pgrad* 2014 - 15**	Logarithmic coefficients for precipitation gradient	−5 (−4.97 – −5.10) −43.1 (−43.19 – −43.28)	—	**−40.7 41.8**	mm $\%^{-1}$
$\boldsymbol{P_T}$	Air temperature threshold to distinguish between solid and liquid precipitation	1 (−1.5 – 3.5)	°C	**−2.3**	mm $°C^{-1}$

Continues

Table IV. (*Continued*)

Name	Description	Calibrated value (plausible range)	Units	Sensitivity of total annual runoff to parameter variations	Units
Glacial meltwater routing (*step 5*)					
k_{ice}	Storage constant for ice melt	2.4	h	0	mm $\%^{-1}$
k_{snow}	Storage constant for snowmelt	10.7	h	0	mm $\%^{-1}$
Snow redistribution by gravity (Ragettli *et al*., 2015)					
SGR_a	Exponential regression function	0.17245	—	−0.9	mm $\%^{-1}$
SGR_C	Snow holding depth dependent on the slope angle	250	m	0.1	mm $\%^{-1}$
Melt delay at the beginning of the season (Fatichi *et al*., 2015; Ragettli *et al*., 2015)					
MeltOnsetTimesteps	Melt delay at the beginning of the season	168	h		
MeltOnsetTemp	Threshold temperature for melt delay at the beginning of the season	0	°C		

the ratio between the daily incident radiation (1° × 1°, NASA product) and the potential radiation was used to compute cloud transmittance factors, which were considered uniform for the entire catchment.

Calibration and validation strategy

The period of analysis of our study is 1 April 2012 to 31 March 2015. This period includes the two monitored years (2013–2014 and 2014–2015) plus the year 2012–2013, which was simulated in order to reach a model state independent from arbitrarily selected initial conditions. Because of the limited extension of our dataset and our focus on reproducing processes in the best possible manner we did not use a traditional division between calibration and validation periods and instead we defined a strategy based on the work of Ragettli and Pellicciotti (2012) and Ragettli *et al*. (2015) (Figure 2). In this way, field measurements that represent a single hydrological process were used to calibrate the parameters controlling that process and were not further modified during the calibration of parameters that resulted from the integration of several processes at the glacier or catchment scale. For example, the parameters *Tmod* and $Tmod_{debris}$ were calibrated exclusively using mean temperature differences between on and off glacier AWSs. On the other hand, field measurements that result from the interaction of several processes were mostly used as validation datasets. For example, time series of distributed albedo measurements were used for validation because they depend on snow accumulation, melt processes and albedo decay. When we calibrated a parameter that integrates the influence of many other processes, we did not modify the previously calibrated parameters. In contrast to common hydrological practice, and also considering our limited amount of streamflow data, we did not use runoff to calibrate model parameters related to distribution of meteorological variables or melt processes. In this way, we can minimize equifinality problems that typically arise in hydrological modelling from the use of single-variable calibration schemes (Beven and Binley, 1992; Beven, 2006; Kirchner, 2006).

The detailed conceptual scheme of this procedure is shown in Figure 2. In step 1, we calculated monthly average temperature gradients using the off-glacier DGA weather network, and we calibrated *Tmod* and $Tmod_{debris}$ using the average differences between on-glacier and off-glacier AWSs. In step 2, we derived the ETI and D-ETI parameters using as reference hourly melt rates calculated with a point-scale energy balance model at the AWSs on Bello and Piramide glaciers. The energy balance model at Bello AWS was run for the period 15 November 2013 to 20 January 2014 and at Piramide AWS for the period March 2015, when snow was absent. The parameters controlling the albedo of snow covered grid cells (a_{max} and r_d) were calibrated using albedo data from the AWS on Bello Glacier in 2014–2015, as this period had a higher variability in albedo values. In step 3, we calibrated precipitation gradients using DGA meteorological stations and the manual snow depth measurements. In step 4, we validated the results from the first three steps using

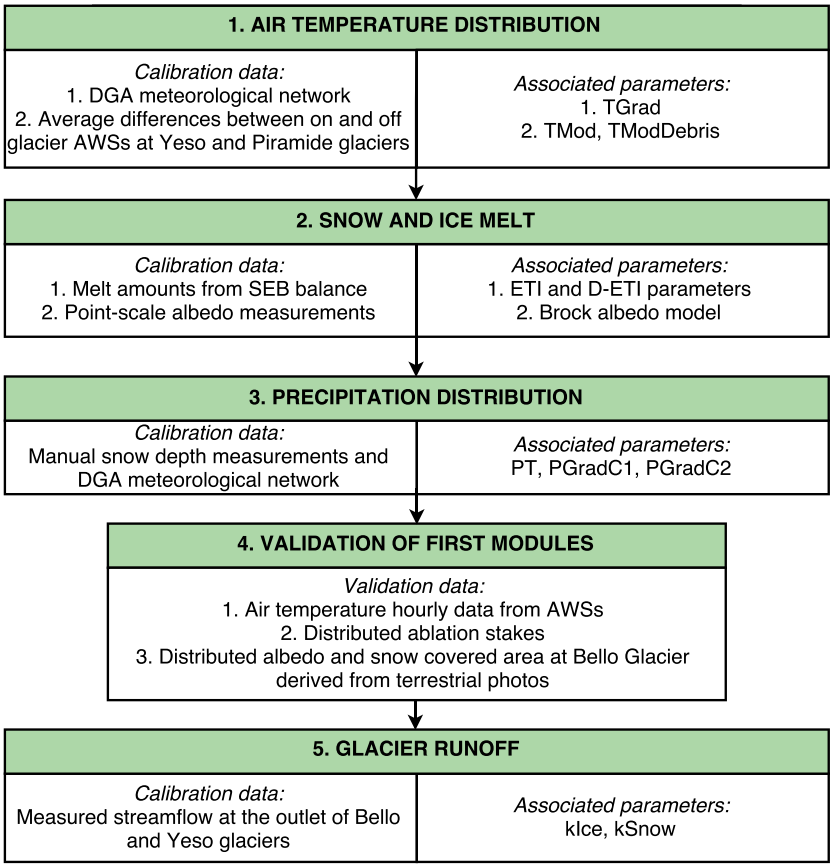

Figure 2. Strategy followed to calibrate the parameters values of TOPKAPI-ETH and to validate its results. Each step of this methodology has a calibration or validation dataset and, in the case of calibration steps, a set of associated TOPKAPI-ETH parameters

hourly temperature measurements at each AWS, the ablation stakes network and time series of distributed albedo and snow cover area derived from the time-lapse camera. Finally, in step 5, we calibrated the storage coefficients of the snow and ice surfaces using streamflow data at the outlets of Bello and Yeso glaciers.

ADDITIONAL METHODS

Debris cover thickness estimation

We derived a debris thickness map (Figure 3) using the methodology proposed by Rounce and McKinney (2014). In this method, a cloud-free thermal satellite image is used to estimate distributed surface temperature, which is then used to solve the surface energy balance in every grid cell of the glacier area. A detailed description of this method is provided in Appendix A1.

Bello and Yeso glaciers show patches of thin debris (<5 cm) with some areas of thick debris at the glacier terminus (>20 cm). Piramide Glacier is completely debris covered with some areas of thin debris (<5 cm) in the upper section, but more than half of the glacier is covered by a debris layer thicker than 10 cm. We compared these results to the dataset of point debris thickness measurements (Figure 3) and found that the observations are well reproduced for debris thickness thinner than 20 cm and the results largely capture observed spatial variability. The agreement for greater thickness is not good. This might be because of the model failing, as with greater sediment thickness surface temperature becomes less dependent on sediment thickness (Schauwecker *et al.*, 2015), and to errors in the observations for thicker measurements.

Reconstruction of albedo from terrestrial photos

We used the method by Corripio (2004) to estimate distributed albedo on Bello Glacier from the daily photographs taken by the time-lapse camera. All cloud-free photographs were georeferenced using the camera position and settings in conjunction with the DEM of the area. Reflectance values were converted to albedo using point albedo measurements at the AWS, atmospheric transmissivity (calculated using the software MODTRAN (Berk *et al.*, 2008)), estimations of diffuse and direct irradiation and the sky view factor of each pixel.

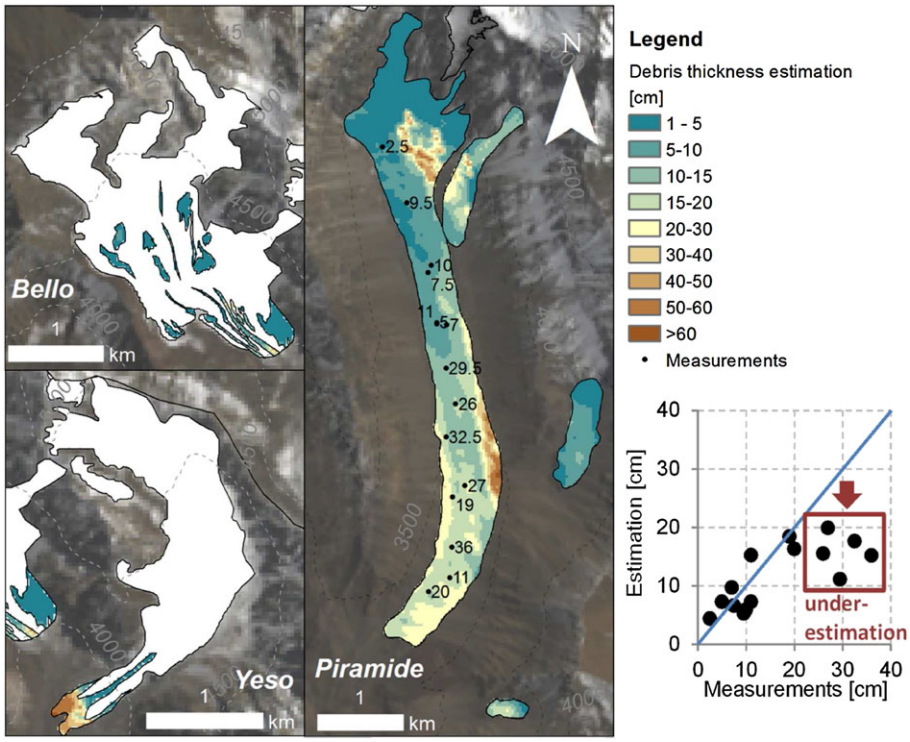

Figure 3. Debris cover thickness map derived using Rounce and McKinney (2014) method from the LANDSAT 8 image. We show Bello, Yeso and Piramide glaciers and three rock glaciers to the east of Piramide Glacier

Additionally, we estimated the snow covered area of the monitored surface assuming a threshold of 0.3 in the albedo values to distinguish between snow-free and snow-covered areas.

Sensitivity and uncertainty analysis

To evaluate the accuracy of model results, we performed a sensitivity analysis of model outputs to parameter variations, as well as an uncertainty analysis of model results. We calculated the sensitivity of total annual runoff to parameter variations for the 2014–2015 hydrological year following the approach of Anslow *et al.* (2008) as used by Ragettli and Pellicciotti (2012) and Heynen *et al.* (2013). This analysis corresponds to a 'one-at-a-time' approach, in which sensitivity coefficients were calculated by varying each parameter by a given amount, calculating the corresponding change in runoff and then fitting a second-order polynomial to the obtained set of values (for details of the curve fitting see Figure 4 in Ragettli and Pellicciotti (2012)). The sensitivity coefficient is the slope of the tangent to the polynomial in correspondence to the initial set. In this way, we calculated the rate of change of the output variable to variations in the individual parameter values and identified the most sensitive parameters. Additionally, for each parameter, we selected the values for which the total annual runoff varies by less than ±5%, to provide a range of plausible parameters that would result in an acceptable model performance.

After identifying the most sensitive model parameters, we performed an uncertainty analysis for the 2014–2015 period. We conducted 250 additional simulations, with each parameter set containing randomly selected parameters within the obtained intervals of acceptable model performance. The parameter selection was performed using Sobol' quasi-random number generator to efficiently sample the parameter space (Bratley and Fox, 1988). Uncertainty ranges of model outputs are provided using the median and the standard deviation of the 250 additional simulations.

RESULTS

Calibration and validation

Overall model calibration provided a good agreement between modelled and measured quantities, and so the calibrated parameters can be assumed to be adequate for use within the modelled basin over the study period (Table IV). The results of each calibration step are outlined below.

The calibration of air temperature distribution (Step 1, Figure 2) showed that air temperature lapse rates are steeper during summer (Table IV), which is consistent

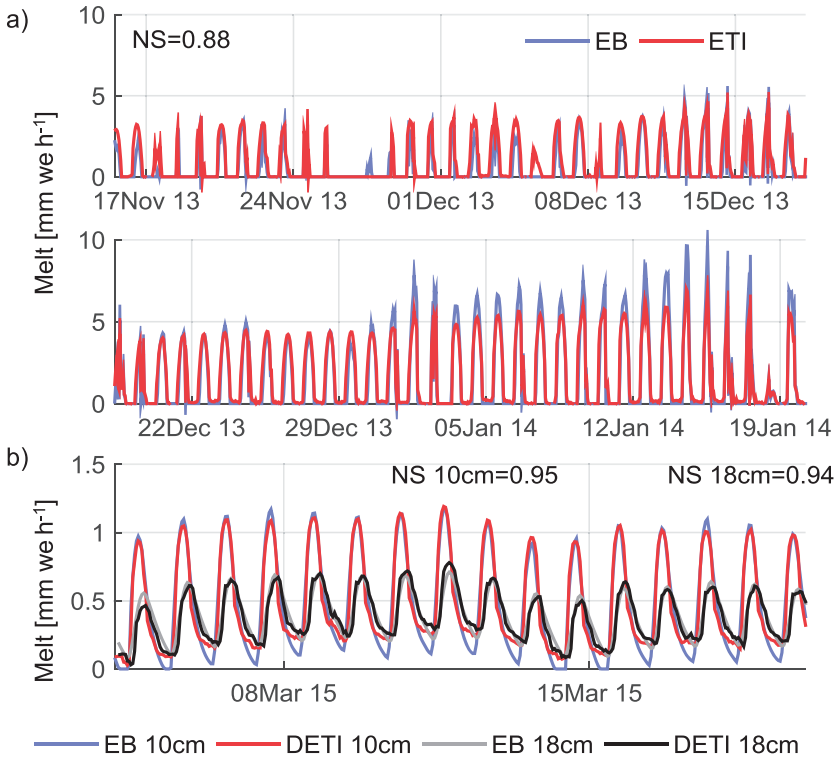

Figure 4. Calibration of melt parameters (Step 2, Figure 2). (a) Calibration of the ETI model using hourly melt rates from an energy balance model as reference. The calibration procedure was performed using data from the AWS on Bello Glacier during the ablation season 2013–2014. We obtained a Nash–Sutcliffe coefficient of 0.88. (b) Calibration of the D-ETI model for different debris thicknesses. Reference melt amounts come from an energy balance model (EB) ran with data from the AWS on Piramide Glacier during the ablation season 2014–2015. The site has a debris thickness of 18 cm. We obtained Nash–Sutcliffe values of 0.95 and 0.94 for a debris thickness of 10 and 18 cm, respectively

with previous studies in alpine regions (Rolland, 2003; Blandford *et al*., 2008). Calibration of the ETI and D-ETI parameters (Step 2, Figure 2) shows a relatively good agreement between reference and simulated melt rates (Nash-Sutcliffe >0.88, Figure 4; Table IV). Figure 5a shows results of the calibration of precipitation gradients using the snow depth measurements (Step 3 of Figure 2). Snow depth measurements at Bello and Piramide glaciers can only be reproduced by using negative relationships with elevation (Table IV). Precipitation at the outlet of the catchment was approximately three times higher than that at the base station, a value that is consistent with the literature (Favier *et al*., 2009; Ragettli *et al*., 2013a), resulting in an increasing trend below 3000 m asl and a decreasing trend above this elevation.

Results from the model validation (Step 4, Figure 2) indicate a relatively good agreement between observed and simulated hourly values of air temperature over the studied glaciers. Simulated air temperatures on Piramide Glacier show the best agreement with observations ($R^2 = 0.92$), suggesting that variations of air temperature induced by the debris-covered glacier boundary layer are relatively small in comparison to the ones induced by the boundary layer over debris-free glaciers (as described in Brock *et al*. (2010)). Simulations of air temperature at Bello and Yeso glaciers show a poorer agreement (R^2 values of 0.5 and 0.76, respectively), particularly at the high-elevation location of Yeso AWS (4428 m asl), which is probably because of complex interactions of synoptic systems and local glacier winds that undermine the assumption of uniform lapse rates (Shea and Moore, 2010; Petersen *et al*., 2013; Ayala *et al*., 2015). In the second validation step, we compared ablation at the ablation stakes and modelled by TOPKAPI-ETH (Figure 5b). While the medians of the observations are well reproduced by the model, the spatial variability is not always captured. This can be related to errors in the estimated debris cover thickness map, the simulation of the end-of-winter snow accumulation or differences between the local and the 30-m scale of the DEM. The final validation step was performed using distributed albedo maps derived from the terrestrial time-lapse camera (Figure 6). There is an overall good correspondence between observed and simulated values for year 2014–2015, but results were poorer for year 2013–2014 when fewer photographs were available (not shown). Many reasons could explain the differences in observed and simulated albedo, including precipitation gradients not appropriate for specific events, air temperature

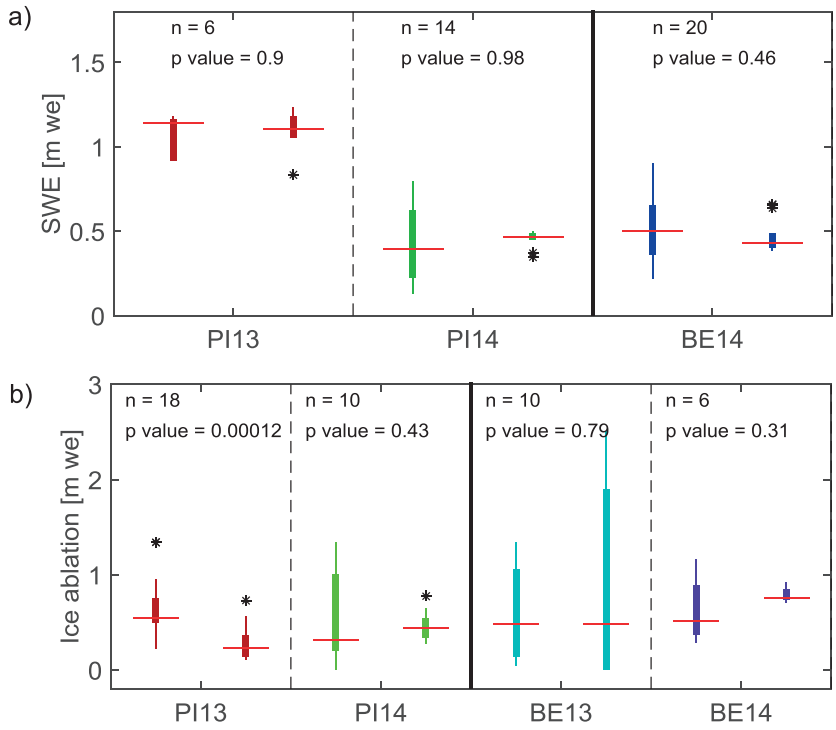

Figure 5. (a): Calibration of precipitation gradients (Step 2, Figure 2). TOPKAPI-ETH simulated values of snow depth compared to observed values at Piramide (PI) and Bello (BE) glaciers during 2013 and 2014. (b) Validation of ice ablation amounts (Step 4, Figure 2). TOPKAPI-ETH simulated values of ice ablation compared to observed values along Piramide (PI) and Bello (BE) glaciers during 2013 and 2014. At each site and season, left and right boxplots represent observed and simulated values, respectively. In both plots, medians are shown as horizontal red lines and outliers as black asterisks. We also show the number of observations (n) used to produce the boxplots and the *p*-value of the Wilcoxon non-parametric test for equal medians with a significance level of 5%. The test cannot reject the null hypothesis of equal medians for all the shown comparisons except for the ice ablation at Piramide 2013 (PI13)

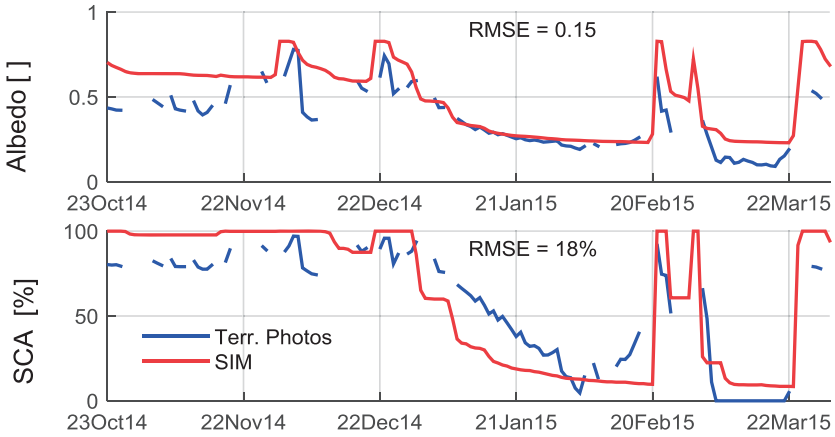

Figure 6. Validation of distributed surface albedo (Step 4, Figure 2). Comparison of observed and simulated time series of mean albedo and snow-covered area over the area monitored using the terrestrial camera at Bello Glacier. Albedo was spatially averaged over the area observed by the camera. A threshold of 0.3 was used to distinguish between snow-covered and snow-free grid cells. RMSE values are indicated in the plots

gradients not appropriate at that time and/or parameters controlling melt and albedo decay that were not valid for the specific meteorological conditions.

Finally for the calibration of glacier runoff (Step 5, Figure 2), we found a good agreement between observed and simulated values of streamflow, but there is probably uncertainty in these parameters, because the data used for calibration are scarce (Figure 7).

Glacier mass balance

Figure 8 shows the annual glacier mass balance of each year as a function of elevation and debris-free and debris-

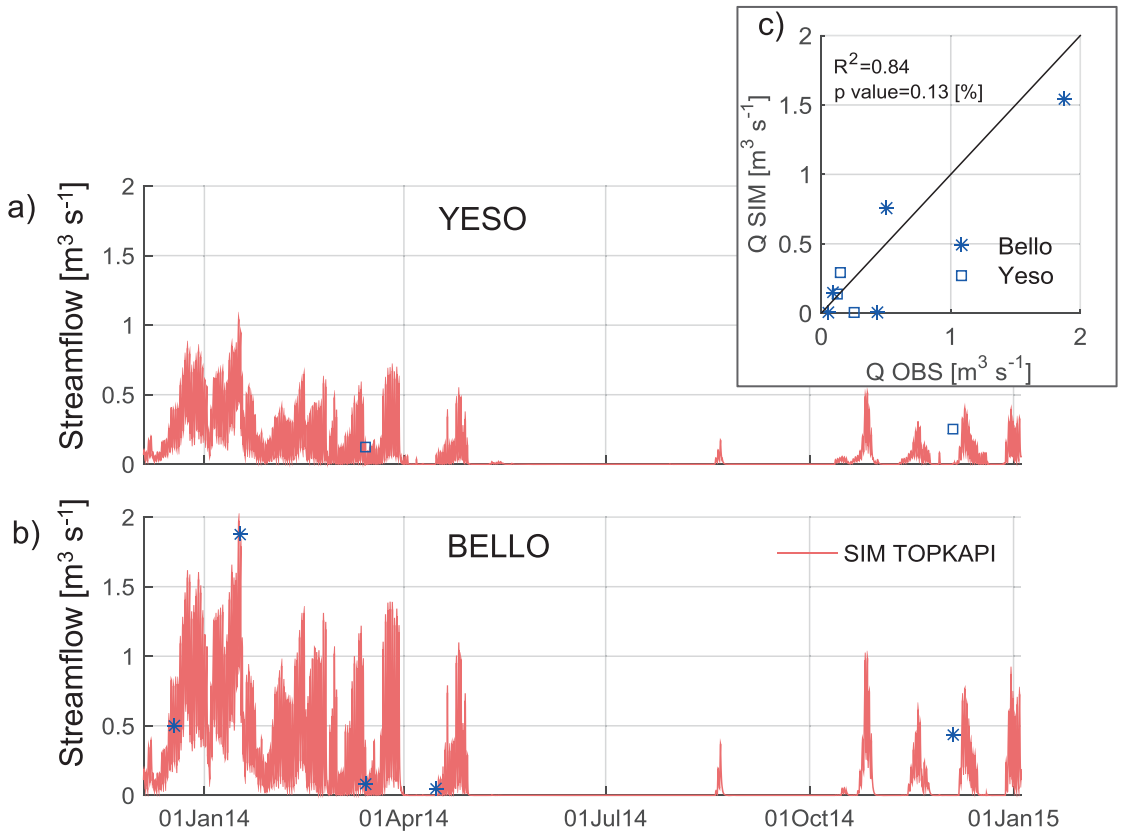

Figure 7. Calibration of water storage coefficients of snow and glacial ice (Step 5, Figure 2). (a-b) TOPKAPI-ETH simulated values of glacier streamflow were compared to individual observations at the outlet of Yeso and Bello glaciers. (c) Scatter plot of simulated and observed values. The p value of the R^2 coefficient corresponds to the probability of getting the observed correlation by random chance, when the true correlation is zero. Note that the last observation at Bello and Yeso glaciers was not captured by the model, probably because of lateral or groundwater runoff contributions

covered areas. In 2013–2014, 51% more precipitation was registered at El Yeso reservoir than in 2014–2015. As a result, TOPKAPI-ETH shows a less negative mass balance during that season.

The mass balance patterns of Bello (Figure 8a) and Yeso (Figure 8b) are remarkably distinct from that of Piramide (Figure 9c). While the mass balance of the former has a clear relation with altitude, with an approximate linear trend above the debris-covered patches at the terminus, the mass balance profile of the debris-covered Piramide Glacier is non-linear, with less negative mass balance at the lower elevations and is increasingly negative with higher elevation, where debris becomes thinner favouring higher melt rates (from 3200 to 3800 m asl). In the upper reaches (from approximately 4100 m asl), where the debris cover is thinner, the usual profile is re-established, such that the mass balance is less negative at higher elevations following an approximately linear behaviour.

To quantify the effect of snow avalanches on the glacier mass balance, we ran a simulation of the model with the snow gravitational distribution module switched off. Figure 8 shows that snow gravitational redistribution can change the local mass balance considerably, turning it from negative to positive, especially in the upper part of Piramide between 3800 and 4200 m asl. Above this glacier section, we observe the opposite effect; high-elevation steep areas lose mass. The effect of avalanches is more pronounced in 2013–2014 than in 2014–2015 because of the higher precipitation amount received during the former period. Mass balance is considerably more negative when avalanches are not included because of the contribution of snow from non-glacierized steep areas (Figure 8d), especially in the higher precipitation year 2013–2014. The effect on the mass balance profile is important for Piramide Glacier in particular, because of its lower elevation where temperatures are higher.

In Figure 8d and Table V, we show a summary of total glacier mass balance and the equilibrium line altitude (ELA) for both years with and without avalanches. The glaciers have mostly negative annual mass balances; however, Bello and Yeso glaciers were close to a neutral mass balance in 2013–2014. ELAs are between 4400 and 4900 m asl for these debris-free glaciers. These values define an accumulation area between one half and one third of the total glacier size. As the mass balance of a

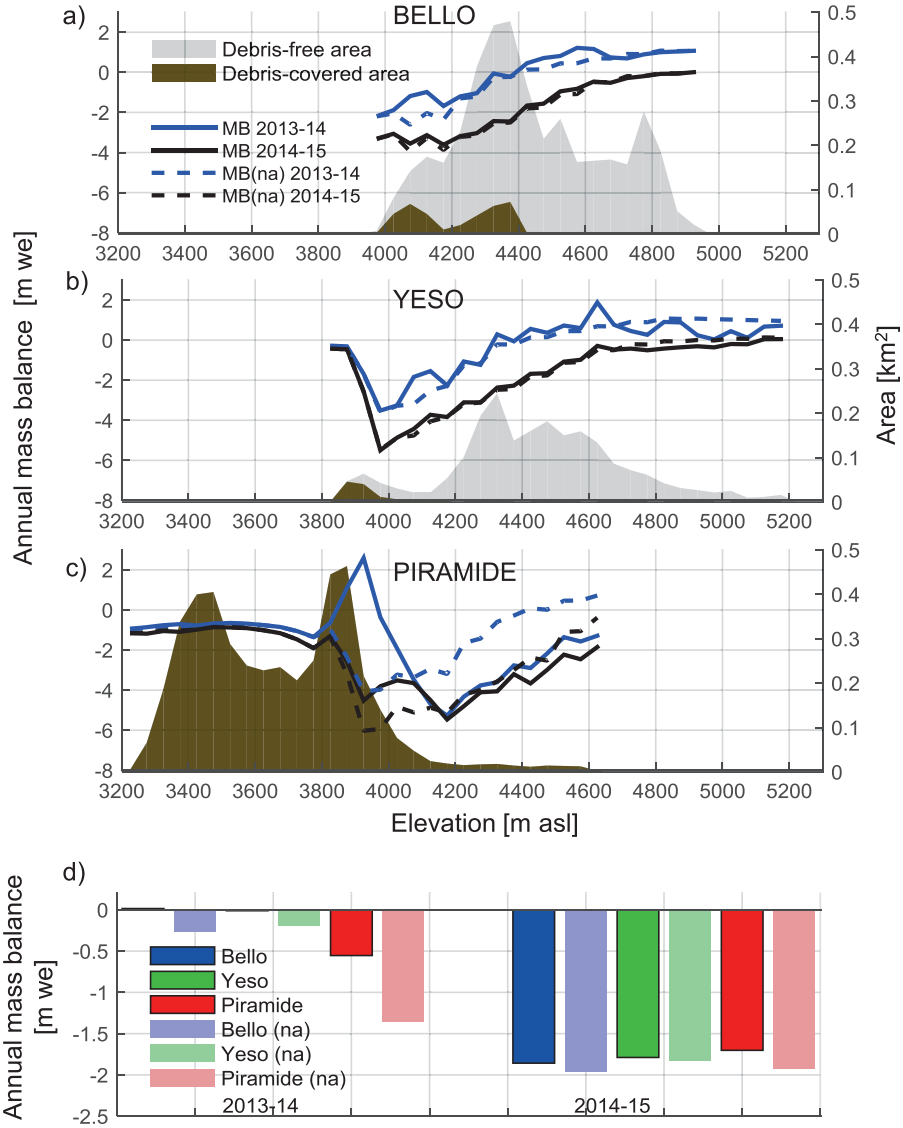

Figure 8. (a) to (c) Simulated annual glacier mass balance of both years as a function of elevation and debris-free and debris-covered areas in Bello, Yeso and Piramide glaciers. Bold and dashed lines represent the mass balance resulting from simulations with and without the snow gravitational redistribution module, respectively. (d) Total glacier mass balance for both analysed seasons. At each glacier, the left (dark colour) and right bars (light colour) represent the mass balance resulting from simulations with and without the snow gravitational redistribution module, respectively

debris-covered glacier is not controlled by elevation, it is difficult to define the ELA for Piramide Glacier. We found values between 3800 and 4100 m asl, but these values are strongly influenced by the mass gravitational redistribution.

Streamflow and runoff components

Figure 9 (a–d) shows simulations of daily discharge at the outlet of Bello, Yeso and Piramide glaciers from the ice and snow reservoirs of TOPKAPI-ETH. Differences between the two years are evident: while snowmelt dominates discharge in 2013–2014 (Figure 9a and 9b), ice melt is more important in 2014–2015 (Figure 9c and 9d). Because of its lower elevation, snow and ice melt from Piramide Glacier starts one or two months earlier than in Bello and Yeso glaciers. By the end of summer, the contribution of ice melt to discharge at Piramide Glacier is of comparable magnitude to the one of Bello and Yeso glaciers, which are located at considerable higher elevations, but with ice surfaces directly exposed to the atmosphere. Annual averages of runoff are shown in Figure 9e. Piramide Glacier contributes the most to runoff, particularly in 2013–2014 (Figure 9a). However, in the drier year 2014–2015, the contribution of Bello and Yeso glaciers increases. When we plot the specific runoff generated from each glacier (Figure 9b), it becomes clear that all glaciers contribute in a similar magnitude.

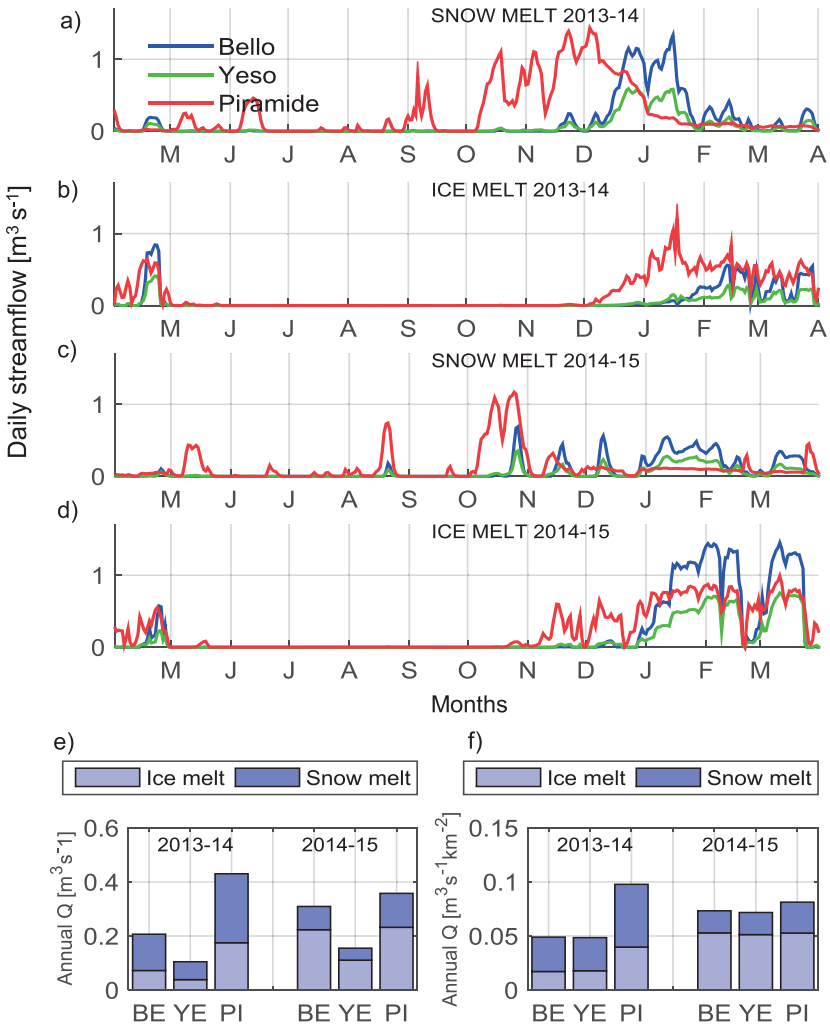

Figure 9. (a–e) Daily mean streamflow from snow and ice melt simulated by TOPKAPI-ETH for Bello, Yeso and Piramide glaciers in the two analysed years. (e) and (f) show an annual summary of these results for runoff and specific runoff (normalized by the glacier areas)

Table V. Simulated glacier mass balances and ELAs.

Glacier	Total mass balance with avalanching[m]		Total mass balance without avalanching[m]		ELA [m asl]	
	2013–2014	2014–2015	2013–2014	2014–2015	2013–2014	2014–2015
Bello	0.02	−1.86	−0.27	−1.96	4419	4775
Yeso	−0.01	−1.79	−0.19	−1.83	4469	4848
Piramide	−0.55	−1.70	−1.35	−1.93	3881	4050

Figure 10 shows the contribution of snowmelt (on and off glacier), glacier ice and liquid precipitation to catchment runoff. Snow cover is the main contributor to runoff in both years, but ice melt can increase from 15% in a snow-rich year such as 2013–2014 to 35% in 2014–2015 and to more than 50% during the austral summer (Figure 10b). The contribution of rain is negligible in both years.

Sensitivity and uncertainty analyses

The sensitivity analysis showed that the model is most sensitive to *Tgrad*, *SRF*, T_T, a_{max}, *Pgrad_C*1 and *Pgrad_C*2 (Table IV). Figure 11 shows uncertainty ranges for the results of Figures 8d, 9e, 9f and 10b for year 2014–2015. Differences in the normalized runoff contribution (Figure 11b) and mass balances (Figure 11c)

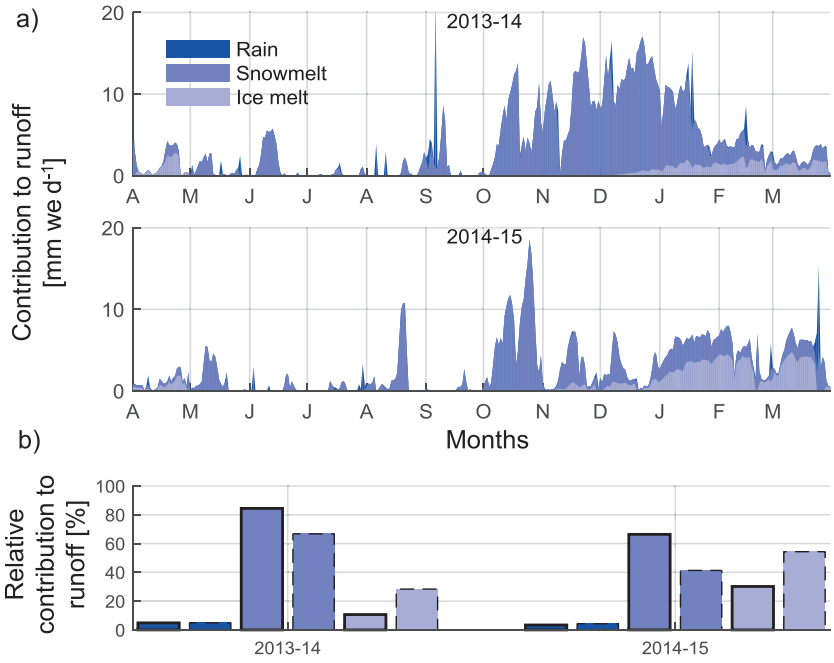

Figure 10. Summary of contributions to runoff simulated by TOPKAPI-ETH. a) Daily total contribution of rain, snowmelt and ice melt to the catchment runoff during years 2013–2014 and 2014–2015. (b) Annual and summer relative contributions of rain, snowmelt and ice melt. At each runoff component left (bold edges) and right bars (dashed edges) represent annual and summer contributions

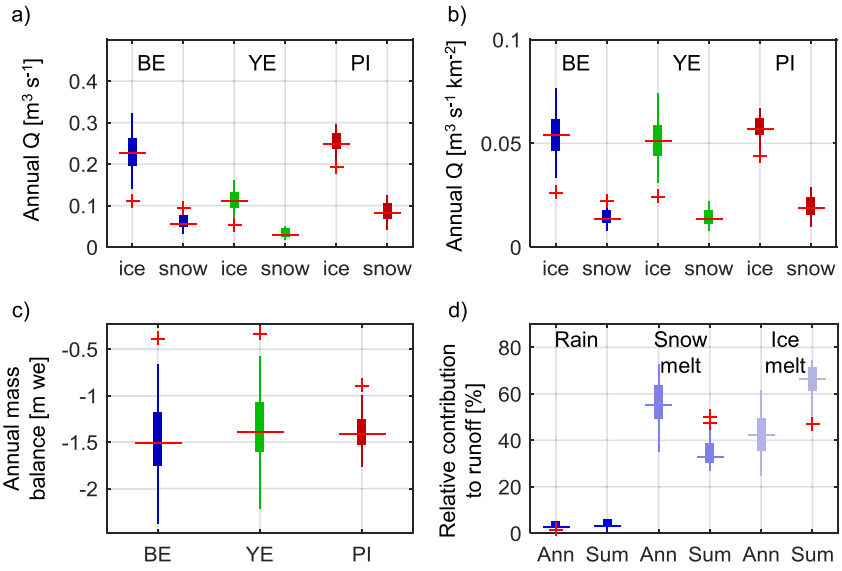

Figure 11. Results of the uncertainty analysis. Each boxplot represents the distribution of the 250 simulations of year 2014–2015 randomly varying the most sensitive parameters within ranges specified at Table IV. (a) Runoff from the snow and ice water storages. (b) Specific runoff from the snow and ice water storages. (c) Annual mass balances. (d) Relative contribution to runoff of each component (rain, snow and ice) at the annual (Ann) and summer (Sum) scales

of the three glaciers are not significant when uncertainty estimates are included. Figure 11d shows that the ice melt contribution to the catchment runoff is 42 ± 8% during the entire year and 67 ± 6% during the summer season (January to March).

DISCUSSION

Mass balance and runoff results

The mass balance pattern of Bello and Yeso glaciers, with an approximate linear relation with elevation, agrees

with findings from debris-free glaciers in other regions of the world (Vincent, 2002; Huss *et al*., 2008; Wagnon *et al*., 2013). We found that ELAs in the debris-free glaciers are between 4400 and 4900 m asl, some of which are higher than what Ragettli *et al*. (2013a) obtained for Juncal Norte Glacier at the end of the 2009 summer (4500 m asl) and that which Carrasco *et al*. (2005) estimated for the region using radiosonde data at the end of the 20th century (4200 m asl). This might be because of either differences in glacier characteristics and elevation in particular, or to the retreat of the ELA to higher altitudes in the most recent period (Mernild *et al*., 2015). The ELA in Piramide Glacier is considerably lower (between 3800 and 4100 m asl), which is consistent with results from other debris-covered glaciers (Ragettli *et al*., 2015), but it is difficult to properly define an ELA when the elevation is not the main control on the mass balance. In a recent study, Mernild *et al*. (2015) found that during the period 2003–2012 the average annual mass balance of glaciers in the central Andes was about -0.86 ± 0.25 m water equivalent (we). This value is close to the average mass balance of the two years analysed in this study, which is -1.0 ± 0.11 m.

Avalanches play a key role for all glaciers but especially at Piramide Glacier, where the low-lying tongue is fed by large avalanches from the steep walls surrounding the upper glacier (Ferrando, 2012). Debris-covered glaciers in many regions of the world are avalanche-fed, but the actual contributions of avalanches to total mass balance and melt have been rarely quantified (Ragettli *et al*., 2015), and this is the first study that shows this effect at play for the Andes of Chile. Our results show that neglecting the avalanche-redistributed snow can affect modelled mass balance results considerably, as avalanches can modify the sign of local mass balances. Simulation of avalanches thus seems an important component for glacio-hydrological models applied to the high relief glacierized catchments of the Andes of Chile.

It is clear from our reference simulation that snowmelt is, at the scale of the catchment investigated, the most important contributor to total runoff, with 84% and 66 % in 2013–2014 and 2014–2015, respectively. Nevertheless, ice melt is an important source of water in dry years (30% in 2014–2015) and summer. These results for the ice melt contribution are higher than those of Ragettli and Pellicciotti (2012) using the same model for year 2005–2006 in Juncal Norte River catchment (14% of total annual runoff), but the contribution of ice melt is lower than the one calculated by Ohlanders *et al*. (2013) for the unusually dry year of 2011–2012 (50–90% of total annual runoff). The contribution to runoff of ice melt during summer is about 54% in 2014–2015, which is lower than the numbers found by Peña and Nazarala (1987) for summer 1968–1969 at a much lower elevation. However, it is difficult to establish whether this is because of differences in the methodology or the climatic conditions of those periods or a combination of both. We have also demonstrated that glacier melt depends on the characteristics of the glaciers, elevation range and surface features, so that any generalisations should be made with caution. Instead, it seems important to repeat such integrated data-rich and modelling studies for other catchments with similar availability of ground observations to establish regional patterns of glacier and runoff changes.

Sources of uncertainty

TOPKAPI-ETH parameters have been calibrated using extensive, local, *in-situ* collected data sets to avoid error compensation and parameter ambiguity, a problem that arises when numerous parameters are calibrated only against one or two integrated catchment-response variables, such as runoff and/or snow cover (Finger *et al*., 2011; Pellicciotti *et al*., 2012). The good agreement between measured and calculated quantities indicates that the model can accurately reproduce several key processes that contribute to the hydrological response of the catchment and is therefore appropriate to characterize Andean catchments. Nevertheless, there remain three main sources of uncertainty in our study: the spatial distribution of forcing variables, the debris thickness reconstruction and the seasonal variability of the calibrated parameters.

While the altitudinal gradients might be able to reproduce precipitation at large, regional scales, they are likely unable to reproduce the complex spatial patterns on rough, high-elevation catchments (Molotch *et al*., 2005; Lehning *et al*., 2011). Our observations of snow water equivalent were particularly low at high elevations, suggesting the action of snow removal by wind, more local complex patterns of precipitation deposition or sublimation losses. A more in-depth understanding of precipitation variability at high elevation would reduce uncertainty in hydrological simulations.

The calculated mass balance and runoff of Piramide Glacier depend primarily on the accuracy of the derived debris thickness map. The major strength of the method used in this study to derive the debris thickness is the use of physically based equations and, in our application, the use of *in-situ* data. However, temperature profiles within the debris, the rate of heat storage and turbulent heat fluxes can create large uncertainties, which significantly increase with a thicker debris cover. While estimated thicknesses at Piramide Glacier are plausible and within the observed range, they might be subjected to uncertainties and values might be too thin in the upper sections

(Schauwecker *et al*., 2015). For these reasons we tested the sensitivity of our results to changes in the debris thickness, finding that variations of ±20% and ±10 cm produce changes of about ±10% and ±50% in the simulated ice melt of the catchment (with thicker debris producing less melt). These results confirm that the model is highly sensitive to debris thickness and the total runoff from Piramide Glacier might be subject to large uncertainties. However, we have confidence in our estimates because of the good model performance in the validation at ablation stakes along the entire length of the glacier.

The adopted stepwise calibration approach attempts to minimize the uncertainty in model parameters by calibrating them against direct measurements of glacio-hydrological processes. However, a limitation of our calibration strategy is that parameters were held constant over the calibration period. This guarantees that they are representative of average conditions over the period of investigation, but also results in a loss of information content. During periods when the snowpack temperature drops below 0 °C or processes other than melt become important to the mass balance (such as snow sublimation), the performance of the ETI model decreases if parameters are not recalibrated for those conditions (Ayala *et al*., 2016). Indeed, the ETI model overestimates daily melt peaks during the first half of the simulated period and compensates by underestimating daily peaks in midsummer (Figure 5a).

In addition to these three sources of uncertainty, there are two processes that were not explicitly considered by the model, which can be relevant for this region. These processes are snow sublimation and the hydrological significance of rock glaciers. Snow sublimation amounts for approximately 20% of total ablation above 4500 m asl (Pellicciotti *et al*., 2008; Ayala *et al*., 2016) and should therefore not strongly affect the simulations in this study (50% and 83% of the catchment is below 4000 and 4500 m asl, respectively). However, the errors induced by neglecting snow sublimation may be compensated by other parameters in the model, and snow sublimation amounts could have a relevant role for the highest sites and for the long-term modelling of glacier mass balance.

Because of a basic lack of understanding, a parameterization of the hydrological contribution of rock glaciers has not been yet explicitly incorporated into glacio-hydrological models. Additionally, the method of Rounce and McKinney (2014) to estimate debris thickness was not developed for rock glaciers. However, it should be noted that rock glaciers in the catchment are small (less than 7.9% of total glacierized area) and are located above 3600 m asl. Future studies should aim to understand the hydrological behaviour of these features and provide numerical models, especially for long-term simulations, but in the absence of an explicit parameterization the treatment of rock glaciers as debris-covered glaciers might give a reasonable approximation of their contribution to runoff.

CONCLUSIONS

We have presented the first modelling comparison of the response to present climate of debris-covered and debris-free glaciers in the Andes of central Chile. We used for this a physically oriented and distributed glacio-hydrological model which was set, calibrated and validated using an extensive data set of *in-situ* observations. To our knowledge, this is one of the few existing modelling studies in the central Andes of Chile, and the first that takes into account explicitly the role of debris-covered glaciers. Our main conclusions are as follows:

a. Debris-covered and debris-free glaciers exhibit remarkably different spatial patterns of mass balance. A positive altitudinal gradient of mass balance is evident for the debris-free Bello and Yeso glaciers, which suggests a connection to air temperature lapse rates. On the other hand, the debris-covered Piramide Glacier mass balance shows, overall, no variation with altitude. On this glacier, piecewise altitudinal gradients, of negative and positive sign, are controlled by debris cover thickness and avalanching. This result has been observed in other studies based on remote sensing data, but it has never been shown as the result of a process-based model.
b. Despite the different spatial patterns of mass balance, debris-free and debris-covered glaciers have similar magnitudes of total mass balance and runoff contribution. However, they differ remarkably in the timing of runoff contribution as snow and ice melt from the debris-covered Piramide Glacier start approximately four weeks earlier than those of the debris-free glaciers. This result is relevant for water managers interested in the timing and seasonality of freshwater resources.
c. At the catchment scale, snowmelt is the dominant contributor to runoff during both years. However, during the driest year of our simulations, ice melt contributes 42 ± 8% and 67 ± 6% of the annual and summer runoff, respectively.
d. A sensitivity analysis showed that some of the largest uncertainties in our results arise from the distribution of the meteorological forcing and the estimation of the debris thickness. However, the sensitivity of mass balances and runoff contributions from Piramide Glacier to variations in meteorological forcing is considerably lower than the one of debris-free glaciers, confirming previous results that suggested that debris-covered glaciers react more slowly to a changing climate.

The data collection effort performed for this study resulted in a unique dataset that allowed the calibration of a process-based hydrological model, its internal validation in a stepwise manner and a consistent comparative study of three glaciers in the catchment. Given the abundance of debris-covered glaciers in the central Andes, it seems imperative to invest into increasing our understanding of their hydrology, surface features and melt mechanisms. We strongly encourage more studies that combine collection of *in-situ*, detailed datasets with distributed, physically oriented models, to establish in a consistent manner the hydrological response to the current climate of high-elevation Andean catchment as a basis for robust future projections of changes.

ACKNOWLEDGEMENTS

The authors thank everyone at CEAZA and Universidad de Chile involved in data collection, especially Rodrigo Ponce and Alexis Caro. Data were collected within the project 'Modelling the mass balance and water discharges from glaciers of North-Central Chile', funded by the Chilean Water Authority (*Dirección General de Aguas*, DGA), which is kindly acknowledged. Alvaro Ayala acknowledges the Becas Chile scholarship program and Paolo Burlando for support at ETH-Zürich. Shelley MacDonell is supported by FONDECYT Initiation into Investigation (11130484). James McPhee acknowledges FONDECYT grant 1121184. We would like to thank very much three anonymous reviewers for their comments which helped improve the manuscript.

REFERENCES

Anslow FS, Hostetler S, Bidlake WR, Clark PU. 2008. Distributed energy balance modeling of South Cascade Glacier, Washington and assessment of model uncertainty. *Journal of Geophysical Research* **113**(F2): F02019. DOI:10.1029/2007JF000850

Ayala A, Pellicciotti F, MacDonell S, McPhee J, Burlando P. 2016. Melt and sublimation on glaciers of the dry Andes: semiarid high-elevation conditions decrease the performance of empirical melt models. *In Preparation for Water Resources Research*.

Ayala A, Pellicciotti F, Shea JM. 2015. Modeling 2 m air temperatures over mountain glaciers: exploring the influence of katabatic cooling and external warming. *Journal of Geophysical Research, [Atmospheres]* **120**: 1–17. DOI:10.1002/2013JD021272

Azócar GF, Brenning A. 2010. Hydrological and geomorphological significance of rock glaciers in the dry Andes, Chile (27°–33°S). *Permafrost and Periglacial Processes* **21**(1): 42–53. DOI:10.1002/ppp.669

Berk A, Anderson G, Acharya PK, Shettle EP. 2008. MODTRAN 5.2.0.0 user's manual

Bernhardt M, Schulz K. 2010. SnowSlide: a simple routine for calculating gravitational snow transport. *Geophysical Research Letters* **37**(11): 1–6. DOI:10.1029/2010GL043086

Beven K. 2006. A manifesto for the equifinality thesis. *Journal of Hydrology* **320**(1–2): 18–36. DOI:10.1016/j.jhydrol.2005.07.007

Beven K, Binley A. 1992. The future of distributed models: model calibration and uncertainty prediction. *Hydrological Processes* **6**: 279–298.

Blandford TR, Humes KS, Harshburger BJ, Moore BC, Walden VP, Ye H. 2008. Seasonal and synoptic variations in near-surface air temperature lapse rates in a mountainous basin. *Journal of Applied Meteorology and Climatology* **47**(1): 249–261. DOI:10.1175/2007JAMC1565.1

Bodin X, Rojas F, Brenning A. 2010. Status and evolution of the cryosphere in the Andes of Santiago (Chile, 33.5°S.) *Geomorphology* **118**(3–4): 453–464. DOI:10.1016/j.geomorph.2010.02.016

Boisier JP, Rondanelli R, Garreaud RD, Muñoz F. 2015. Anthropogenic and natural contributions to the Southeast Pacific precipitation decline and recent mega-drought in central Chile. *Geophysical Research Letters* DOI:10.1002/2015GL067265

Bown F, Rivera A, Acuña C. 2008. Recent glacier variations at the Aconcagua basin, central Chilean Andes. *Annals of Glaciology* **48**: 43–48. DOI:10.3189/172756408784700572

Bratley P, Fox BL. 1988. ALGORITHM 659: implementing Sobol's quasirandom sequence generator. *ACM Transactions on Mathematical Software* **14**(1): 88–100. DOI:10.1145/42288.214372

Brock B, Rivera A, Casassa G, Bown F, Acuña C. 2007. The surface energy balance of an active ice-covered volcano: Villarrica Volcano, southern Chile. *Annals of Glaciology* **45**: 104–114. DOI:10.3189/172756407782282372

Brock BW, Mihalcea C, Kirkbride MP, Diolaiuti G, Cutler MEJ, Smiraglia C. 2010. Meteorology and surface energy fluxes in the 2005–2007 ablation seasons at the Miage debris-covered glacier, Mont Blanc Massif, Italian Alps. *Journal of Geophysical Research, [Atmospheres]* **115**(9): 1–16. DOI:10.1029/2009JD013224

Brock BW, Willis IC, Sharp MJ. 2000. Measurement and parameterisation of albedo variations at Haut Glacier d' Arolla, Switzerland. *Journal of Glaciology* **46**(155): 675–688. DOI:10.3189/172756506781828746

Buri P, Pellicciotti F, Steiner JF, Evan S, Immerzeel WW. 2015. A grid-based model of backwasting of supraglacial ice cliffs on debris-covered glaciers. *Annals of Glaciology* **57**(71): in press. DOI:10.3189/2016AoG71A059

Carenzo M, Pellicciotti F, Mabillard J, Reid T, Brock BW. 2015. An enhanced debris temperature index model accounting for thickness effect. *Advances in Water Resources* **94**: 457–469. DOI:10.1016/j.advwatres.2016.05.001

Carrasco JF, Casassa G, Quintana J. 2005. Changes of the 0 °C isotherm and the equilibrium line altitude in central Chile during the last quarter of the 20th century. *Hydrological Sciences Journal* **50**(6): 37–41. DOI:10.1623/hysj.2005.50.6.933

Carrasco JF, Osorio R, Casassa G. 2008. Secular trend of the equilibrium-line altitude on the western side of the southern Andes, derived from radiosonde and surface observations. *Journal of Glaciology* **54**(186): 538–550. DOI:10.3189/002214308785837002

Ciarapica L, Todini E. 2002. TOPKAPI: a model for the representation of the rainfall-runoff process at different scales. *Hydrological Processes* **16**(2): 207–229. DOI:10.1002/hyp.342

Comitato-Ev-K2-CNR. 2012. *Plan de Acción para la Conservación de Glaciares ante el Cambio Climático*. Dirección General de Aguas: Santiago.

Cornwell E, Molotch NP, McPhee J. 2016. Spatio-temporal variability of snow water equivalent in the extra-tropical Andes Cordillera from distributed energy balance modeling and remotely sensed snow cover. *Hydrology and Earth System Sciences* **20**(1): 411–430. DOI:10.5194/hess-20-411-2016

Corripio JG. 2004. Snow surface albedo estimation using terrestrial photography. *International Journal of Remote Sensing* **25**(24): 5705–5729.

Cortés G, Vargas X, McPhee J. 2011. Climatic sensitivity of streamflow timing in the extratropical western Andes Cordillera. *Journal of Hydrology* **405**(1–2): 93–109. DOI:10.1016/j.jhydrol.2011.05.013

Demaria EMC, Maurer EP, Sheffield J, Bustos E, Poblete D, Vicuña S, Meza F. 2013. Using a gridded global dataset to characterize regional hydroclimate in Central Chile. *Journal of Hydrometeorology* **14**(1): 251–265. DOI:10.1175/JHM-D-12-047.1

DGA. 2010. Glaciares desde cuencas altiplánicas hasta cuenca del río Petrohué. *Inventario de Glaciares* Available at: http://www.dga.cl/productosyservicios/mapas/Paginas/default.aspx [Accessed 1 June 2015]

Dilley AC, O'Brien DM. 1998. Estimating downward clear sky long-wave irradiance at the surface from screen temperature and precipitable water. *Quarterly Journal of the Royal Meteorological Society* **124**: 1391–1401.

Evatt GW, Abrahams ID, Heil M, Kingslake J, Mitchell SL, Andrew C, Clark CD. 2015. Glacial melt under a porous debris layer. *Journal of Glaciology* **61**(229): 825–836. DOI:10.3189/2015JoG14J235

Fatichi S, Rimkus S, Burlando P, Bordoy R, Molnar P. 2015. High-resolution distributed evaluation of climate and anthropogenic changes on the hydrology of an Alpine catchment. *Journal of Hydrology* **525**: 362–382. DOI:10.1016/j.jhydrol.2015.03.036

Favier V, Falvey M, Rabatel A, Praderio E, Lopez D. 2009. Interpreting discrepancies between discharge and precipitation in high-altitude area of Chile's Norte Chico region (26–32°S). *Water Resources Research* **45** (W02424). DOI:10.1029/2008WR006802

Ferrando F. 2012. Pirámide Glacier: characteristics and evolution of a mantled glacier. Climatic change evidences. *Investigaciones Geográficas Chile* **44**: 57–74.

Finger D, Pellicciotti F, Konz M, Rimkus S, Burlando P. 2011. The value of glacier mass balance, satellite snow cover images, and hourly discharge for improving the performance of a physically based distributed hydrological model. *Water Resources Research* **47**(7): 1–14. DOI:10.1029/2010WR009824

Foster LA, Brock BW, Cutler MEJ, Diotri F. 2012. A physically based method for estimating supraglacial debris thickness from thermal band remote-sensing data. *Journal of Glaciology* **58**(210): 677–691. DOI:10.3189/2012JoG11J194

Fujita K, Sakai A. 2014. Modelling runoff from a Himalayan debris-covered glacier. *Hydrology and Earth System Sciences* **18**(7): 2679–2694. DOI:10.5194/hess-18-2679-2014

Gardelle J, Berthier E, Arnaud Y. 2012. Slight mass gain of Karakoram glaciers in the early twenty-first century. *Nature Geoscience* **5**(5): 322–325. DOI:10.1038/ngeo1450

Gardelle J, Berthier E, Arnaud Y, Kääb A. 2013. Region-wide glacier mass balances over the Pamir–Karakoram–Himalaya during 1999–2011. *The Cryosphere* **7**(4): 1263–1286. DOI:10.5194/tc-7-1263-2013

Gascoin S, Kinnard C, Ponce R, Lhermitte S, MacDonell S, Rabatel A. 2011. Glacier contribution to streamflow in two headwaters of the Huasco River, Dry Andes of Chile. *The Cryosphere* **5**(4): 1099–1113. DOI:10.5194/tc-5-1099-2011

Gascoin S, Lhermitte S, Kinnard C, Bortels K, Liston GE. 2013. Wind effects on snow cover in Pascua-Lama, Dry Andes of Chile. *Advances in Water Resources* **55**: 25–39. DOI:10.1016/j.advwatres.2012.11.013

Greuell W, Böhm R. 1998. 2 m temperatures along melting mid-latitude glaciers, and implications for the sensitivity of the mass balance to variations in temperature. *Journal of Glaciology* **44**(146): 9–20.

Heynen M, Pellicciotti F, Carenzo M. 2013. Parameter sensitivity of a distributed enhanced temperature-index melt model. *Annals of Glaciology* **54**(63): 311–321. DOI:10.3189/2013AoG63A537

Hock R, Noetzli C. 1997. Areal melt and discharge modelling of Storglaciären. *Annals of Glaciology* **24**: 211–216.

Huss M, Bauder A, Funk M, Hock R. 2008. Determination of the seasonal mass balance of four Alpine glaciers since 1865. *Journal of Geophysical Research* **113**(F1): F01015. DOI:10.1029/2007JF000803

Huss M, Jouvet G, Farinotti D, Bauder A. 2010. Future high-mountain hydrology: a new parameterization of glacier retreat. *Hydrology and Earth System Sciences* **14**(5): 815–829. DOI:10.5194/hess-14-815-2010

Immerzeel WW, Kraaijenbrink PDA, Shea JM, Shrestha AB, Pellicciotti F, Bierkens MFP, De Jong SM. 2014. High-resolution monitoring of Himalayan glacier dynamics using unmanned aerial vehicles. *Remote Sensing of Environment* **150**: 93–103. DOI:10.1016/j.rse.2014.04.025

Janke JR, Bellisario AC, Ferrando FA. 2015. Classification of debris-covered glaciers and rock glaciers in the Andes of central Chile. *Geomorphology* **241**: 98–121. DOI:10.1016/j.geomorph.2015.03.034

Juszak I, Pellicciotti F. 2013. A comparison of parameterizations of incoming longwave radiation over melting glaciers: model robustness and seasonal variability. *Journal of Geophysical Research, [Atmospheres]* **118**: DOI:10.1002/jgrd.50277

Kääb A, Berthier E, Nuth C, Gardelle J, Arnaud Y, Kaab A, Berthier E, Nuth C, Gardelle J, Arnaud Y. 2012. Contrasting patterns of early twenty-first-century glacier mass change in the Himalayas. *Nature* **488**(7412): 495–498. DOI:10.1038/nature11324

Kirchner JW. 2006. Getting the right answers for the right reasons: linking measurements, analyses, and models to advance the science of hydrology. *Water Resources Research* **42**(3): 1–5. DOI:10.1029/2005WR004362

Kraaijenbrink P, Meijer SW, Shea JM, Pellicciotti F, De Jong SM, Immerzeel WW. 2016. Seasonal surface velocities of a Himalayan glacier derived by automated correlation of unmanned aerial vehicle imagery. *Annals of Glaciology* **57**(71): 103–113. DOI:10.3189/2016AoG71A072

Larraín S. 2007. Glaciares Chilenos, Reservas estrategicas de agua dulce. *Revista Ambiente y Desarrollo* **23**(3): 28–35.

Lehning M, Grünewald T, Schirmer M. 2011. Mountain snow distribution governed by an altitudinal gradient and terrain roughness. *Geophysical Research Letters* **38**(L19504): 1–5. DOI:10.1029/2011GL048927

Lejeune Y, Bertrand J-M, Wagnon P, Morin S. 2013. A physically based model of the year-round surface energy and mass balance of debris-covered glaciers. *Journal of Glaciology* **59**(214): 327–344. DOI:10.3189/2013JoG12J149

Lhermitte S, Abermann J, Kinnard C. 2014. Albedo over rough snow and ice surfaces. *The Cryosphere* **8**(3): 1069–1086. DOI:10.5194/tc-8-1069-2014

Liu Z, Todini E. 2002. Towards a comprehensive physically-based rainfall–runoff model. *Hydrology and Earth System Sciences* **6**(5): 859–881. DOI:10.5194/hess-6-859-2002

MacDonell S, Kinnard C, Mölg T, Nicholson L, Abermann J. 2013a. Meteorological drivers of ablation processes on a cold glacier in the semi-arid Andes of Chile. *The Cryosphere* **7**(5): 1513–1526. DOI:10.5194/tc-7-1513-2013

MacDonell S, Nicholson L, Kinnard C. 2013b. Parameterisation of incoming longwave radiation over glacier surfaces in the semiarid Andes of Chile. *Theoretical and Applied Climatology* **111**(3–4): 513–528. DOI:10.1007/s00704-012-0675-1

Marangunic C. 1979. *Informe sobre el inventario de glaciares en las subhoyas del río Maipo superior y del estero Angostura*. Dirección General de Aguas: Santiago.

Masiokas M, Villalba R, Luckman B, Le Quesne C, Aravena J. 2006. Snowpack variations in the central Andes of Argentina and Chile, 1951–2005: large-scale atmospheric influences and implications for water resources in the region. *Journal of Climate* **19**: 6334–6352.

Masiokas MH, Villalba R, Luckman BH, Mauget S. 2010. Intra- to multidecadal variations of snowpack and streamflow records in the Andes of Chile and Argentina between 30° and 37°S. *Journal of Hydrometeorology* **11**: 822–831. DOI:10.1175/2010JHM1191.1

Mernild SH, Beckerman AP, Yde JC, Hanna E, Malmros JK, Wilson R, Zemp M. 2015. Mass loss and imbalance of glaciers along the Andes Cordillera to the sub-Antarctic islands. *Global and Planetary Change* **133**: 109–119. DOI:10.1016/j.gloplacha.2015.08.009

Meza FJ, Vicuna S, Gironás J, Poblete D, Suárez F, Oertel M. 2015. Water–food–energy nexus in Chile: the challenges due to global change in different regional contexts. *Water International* **40**(5–6): 839–855. DOI:10.1080/02508060.2015.1087797

Meza FJ, Wilks DS, Gurovich L, Bambach N. 2013. Impacts of climate change on irrigated agriculture in the Maipo basin, Chile: reliability of water rights and changes in the demand for irrigation. *Journal of Water Resources Planning and Management* **139**(October): 554–564. DOI:10.1061/(ASCE)WR.1943-5452

Miles ES, Pellicciotti F, Willis IC, Steiner JF, Buri P, Arnold NS. 2016. Refined energy-balance modelling of a supraglacial pond, Langtang Khola, Nepal. *Annals of Glaciology* **57**(71): 29–40. DOI:10.3189/2016AoG71A421

Molotch NP, Colee MT, Bales RC, Dozier J. 2005. Estimating the spatial distribution of snow water equivalent in an alpine basin using binary regression tree models: the impact of digital elevation data and independent variable selection. *Hydrological Processes* **19**: 1459–1479.

Nicholson L, Marin J, Lopez D. 2010. Glacier inventory of the upper Huasco valley, Norte Chico, Chile: glacier characteristics, glacier change and comparison with central Chile. *Annals of Glaciology* **50**(53): 111–118.

Nuimura T, Fujita K, Yamaguchi S, Sharma RR. 2012. Elevation changes of glaciers revealed by multitemporal digital elevation models calibrated by GPS survey in the Khumbu region, Nepal Himalaya, 1992–2008. *Journal of Glaciology* **58** (Table 1): 648–656. DOI:10.3189/2012JoG11J061

Ohlanders N, Rodriguez M, McPhee J. 2013. Stable water isotope variation in a Central Andean watershed dominated by glacier and

snowmelt. *Hydrology and Earth System Sciences* **17**(3): 1035–1050. DOI:10.5194/hess-17-1035-2013

Pellicciotti F, Brock B, Strasser U, Burlando P, Funk M, Corripio J. 2005. An enhanced temperature-index glacier melt model including the shortwave radiation balance: development and testing for Haut Glacier d'Arolla, Switzerland. *Journal of Glaciology* **51**(175): 573–587. DOI:10.3189/172756505781829124

Pellicciotti F, Buergi C, Immerzeel WW, Konz M, Shrestha AB. 2012. Challenges and uncertainties in hydrological modeling of remote Hindu Kush–Karakoram–Himalayan (HKH) Basins: suggestions for calibration strategies. *Mountain Research and Development* **32**(1): 39–50. DOI:10.1659/MRD-JOURNAL-D-11-00092.1

Pellicciotti F, Helbing J, Rivera A, Favier V, Corripio J, Araos J, Sicart JE, Carenzo M. 2008. A study of the energy balance and melt regime on Juncal Norte Glacier, semi-arid Andes of central Chile, using melt models of different complexity. *Hydrological Processes* **22**: 3980–3997. DOI:10.1002/hyp.7085

Pellicciotti F, Ragettli S, Carenzo M, McPhee J. 2014. Changes of glaciers in the Andes of Chile and priorities for future work. *The Science of the Total Environment* **493C**: 1197–1210. DOI:10.1016/j.scitotenv.2013.10.055

Pellicciotti F, Raschle T, Huerlimann T, Carenzo M, Burlando P. 2011. Transmission of solar radiation through clouds on melting glaciers: a comparison of parameterizations and their impact on melt modelling. *Journal of Glaciology* **57**(202): 367–381. DOI:10.3189/002214311796406013

Pellicciotti F, Stephan C, Miles E, Herreid S, Immerzeel WW, Bolch T. 2015. Mass-balance changes of the debris-covered glaciers in the Langtang Himal, Nepal, from 1974 to 1999. *Journal of Glaciology* **61**(226): 373–386. DOI:10.3189/2015JoG13J237

Peña H, Nazarala B. 1987. Snowmelt-runoff simulation model of a central Chile Andean basin with relevant orographic effects. In *Large Scale Effects of Seasonal Snow Cover* (*Proceedings of the Vancouver Symposium*, *August 1987*).

Peña H, Escobar F, Vidal F. 1985. Procedimiento para la estimación de crecidas en cuencas nivales. In *VII Congreso Nacional de La Sociedad Chilena de Ingeniería Hidráulica*Dirección General de Aguas: Santiago.

Petersen L, Pellicciotti F, Juszak I, Carenzo M, Brock B. 2013. Suitability of a constant air temperature lapse rate over an Alpine glacier: testing the Greuell and Böhm model as an alternative. *Annals of Glaciology* **54**(63): 120–130. DOI:10.3189/2013AoG63A477

Pourrier J, Jourde H, Kinnard C, Gascoin S, Monnier S. 2014. Glacier meltwater flow paths and storage in a geomorphologically complex glacial foreland: the case of the Tapado glacier, dry Andes of Chile (30°S). *Journal of Hydrology* **519**: 1068–1083. DOI:10.1016/j.jhydrol.2014.08.023

Le Quesne C, Acuña C, Boninsegna J a, Rivera A, Barichivich J. 2009. Long-term glacier variations in the Central Andes of Argentina and Chile, inferred from historical records and tree-ring reconstructed precipitation. *Palaeogeography, Palaeoclimatology, Palaeoecology* **281**(3–4): 334–344. DOI:10.1016/j.palaeo.2008.01.039

Ragettli S, Pellicciotti F. 2012. Calibration of a physically based, spatially distributed hydrological model in a glacierized basin: on the use of knowledge from glaciometeorological processes to constrain model parameters. *Water Resources Research* **48**: W03509. DOI:10.1029/2011WR010559

Ragettli S, Bolch T, Pellicciotti F. 2016. Heterogeneous glacier thinning patterns over the last 40 years in Langtang Himal. *The Cryosphere Discussion* (February): 1–53. DOI:10.5194/tc-2016-25

Ragettli S, Cortés G, McPhee J, Pellicciotti F. 2013a. An evaluation of approaches for modelling hydrological processes in high-elevation, glacierized Andean watersheds. *Hydrological Processes*. DOI:10.1002/hyp.10055

Ragettli S, Pellicciotti F, Bordoy R, Immerzeel WW. 2013b. Sources of uncertainty in modeling the glaciohydrological response of a Karakoram watershed to climate change. *Water Resources Research* **49**(9): 6048–6066. DOI:10.1002/wrcr.20450

Ragettli S, Pellicciotti F, Immerzeel WW, Miles E, Petersen L, Heynen M, Shea JM, Stumm D, Joshi S, Shrestha AB. 2015. Unraveling the hydrology of a Himalayan watershed through integration of high resolution in- situ data and remote sensing with an advanced simulation model. *Advances in Water Resources* **78**: 94–111. DOI:10.1016/j.advwatres.2015.01.013

Ragettli SG. 2014. Modeling the response of high-elevation, glacierized watersheds to climate change: a new methodological framework applied to the Andes and the Himalaya. DOI:10.3929/ethz-a-010394813

Rolland C. 2003. Spatial and seasonal variations of air temperature lapse rates in alpine regions. *Journal of Climate* **16**: 1032–1046. DOI:10.1175/1520-0442(2003)016<1032:SASVOA>2.0.CO;2

Rounce DR, McKinney DC. 2014. Debris thickness of glaciers in the Everest Area (Nepal Himalaya) derived from satellite imagery using a nonlinear energy balance model. *The Cryosphere* **8**(1): 1317–1329. DOI:10.5194/tcd-8-887-2014

Rubio-Álvarez E, McPhee J. 2010. Patterns of spatial and temporal variability in streamflow records in south central Chile in the period 1952–2003. *Water Resources Research* **46**(5): 1–16. DOI:10.1029/2009WR007982

Sakai A, Takeuchi N, Fujita K, Nakawo M. 2000. Role of supraglacial ponds in the ablation process of a debris-covered glacier in the Nepal Himalayas. In *Debris-Covered Glaciers*. IAHS: Seattle; 119–130.

Schauwecker S, Rohrer M, Huggel C, Kulkarni A, Ramanathan A, Salzmann N, Stoffel M, Brock B. 2015. Remotely sensed debris thickness mapping of Bara Shigri Glacier, Indian Himalayas. *Journal 0f Glaciology* **61**(228): 1–26. DOI:10.3189/2015JoG14J102

Shea JM, Moore RD. 2010. Prediction of spatially distributed regional-scale fields of air temperature and vapor pressure over mountain glaciers. *Journal of Geophysical Research* **115**(D23): D23107. DOI:10.1029/2010JD014351

Sinclair KE, MacDonell S. 2015. Seasonal evolution of penitente glaciochemistry at Tapado Glacier, Northern Chile. *Hydrological Processes* DOI:10.1002/hyp.10531

Steiner JF, Pellicciotti F. 2016. Variability of air temperature over a debris-covered glacier in the Nepalese Himalaya. *Annals of Glaciology* **57**(71): 295–307. DOI:10.3189/2016AoG71A066

Steiner JF, Pellicciotti F, Buri P, Miles ES, Immerzeel WW, Reid TD. 2015. Modelling ice-cliff backwasting on a debris-covered glacier in the Nepalese Himalaya. *Journal of Glaciology* **61**(229): 889–907. DOI:10.3189/2015JoG14J194

Takeuchi Y, Kayastha RB, Nakawo M. 2000. Characteristics of ablation and heat balance in debris-free and debris-covered areas on Khumbu Glacier, Nepal Himalayas, in the pre-monsoon season. In *Debris-Covered Glaciers*, IAHS: Seattle; 53–61.

USGS. 2015. Landsat 8 (L8) Data Users Handbook. *Earth Resources Observation and Science* (*EROS*) *Center* **8** (June): 97.

Vincent C. 2002. Influence of climate change over the 20th Century on four French glacier mass balances. *Journal of Geophysical Research* **107**(D19): 4375. DOI:10.1029/2001JD000832

Wagnon P, Vincent C, Arnaud Y, Berthier E, Vuillermoz E, Gruber S, Ménégoz M, Gilbert a, Dumont M, Shea JM, Stumm D, Pokhrel BK. 2013. Seasonal and annual mass balances of Mera and Pokalde glaciers (Nepal Himalaya) since 2007. *The Cryosphere* **7**(6): 1769–1786. DOI:10.5194/tc-7-1769-2013

Yates DN, Sieber J, Purkey DR, Huber-Lee A. 2005. WEAP21—a demand-, priority-, and preference-driven water planning model part 1 : model characteristics. *Water International* **30**(4): 487–500. DOI:10.1080/02508060508691893

APPENDIX A1. CALCULATION OF DEBRIS THICKNESS

BACKGROUND

Debris thickness was computed using the method developed by Rounce and McKinney (2014), thereafter called the R14 method, which is an improved version of a methodology proposed by Foster *et al*. (2012), here named the F12 method. The basic principle of both methods is that debris surface temperature during daytime is largely dependent on debris thickness. The influence from other

sources, such as shading, daytime and air temperature can be removed by accounting for those factors and solving the surface energy balance equations for a layer of debris.

In the original model by Foster *et al*. (2012), the ground heat flux G, increased by a stored heat factor F, is the residual of the energy balance:

$$S + L + H + LE = G \cdot (1 + F), \tag{A.1}$$

where S is net shortwave radiation, L is net longwave radiation, LE is the latent heat flux and H is the sensible heat flux.

According to Fick's law of heat diffusion, G can also be expressed as:

$$G = K \cdot \frac{dT}{dz} \simeq K \cdot \frac{T_S - T_{ice}}{d}, \tag{A.2}$$

where K is the effective thermal conductivity, T_S is debris surface temperature, T_{ice} is the temperature of the underlying glacier ice (Tice = 0 °C) and d is debris thickness.

Originally, the F12 method accounts for the effect of heat storage within the debris by introducing a constant heat storage factor $F = 0.64$ and by assuming a linear debris temperature profile. The R14 method introduces the G_{ratio} to correct the simplified assumption of a linear debris temperature profile in the calculation of the ground heat flux G. During the warming of the debris surface by shortwave radiation in the morning hours, the temperature gradient in the uppermost part of the debris layer is very steep, while the gradient remains small or even close to zero in the lower part. By measuring vertical profiles of debris temperature, the G_{ratio} can be computed as the ratio between the debris temperature gradient in the uppermost layer and the debris temperature gradient over the entire debris layer:

$$G_{ratio} = \frac{T_S - T_1}{d_1} \Big/ \frac{T_S - T_{ice}}{d}, \tag{A.3}$$

where d_1 and T_1 are the thickness and the temperature of the uppermost layer. The corrected ground heat flux G becomes:

$$G = G_{ratio} \cdot K \cdot \frac{T_S - T_{ice}}{d} = G_{ratio} \cdot K \cdot \frac{T_S}{d}. \tag{A.4}$$

And the calculation of debris thickness from the inversion of the energy balance is:

$$d = K \cdot T_S \cdot \frac{G_{ratio}}{S + L + H + LE}. \tag{A.5}$$

Thereby, the stored heat factor $F = 0.64$, used in the F12 method, is not needed in this formulation, because the G_{ratio} itself accounts for effects of heat storage.

DATA AND METHODOLOGY

In our study, meteorological data necessary for the energy balance calculations are measured at the AWS on Piramide Glacier. The distributed debris surface temperature is obtained from a LANDSAT 8 satellite thermal image of 60-m resolution retrieved on 22 February 2015. The meteorological data needed as input to the energy balance equation and measured at the location of the AWS need to be distributed to the glacier scale and every pixel. For each satellite image pixel, air temperature was calculated from satellite-borne surface temperature via a partial linear regression, as described by Steiner and Pellicciotti (2016). This allows a much more accurate calculation of the turbulent sensible heat flux and the incoming longwave radiation than if uniform in space air temperature were used as forcing to the model (Equation A.4). Distributed incoming shortwave radiation was computed using the solar radiation module of ArcGIS® software for the exact time and date of the satellite overpass. Incoming longwave radiation was computed using a parameterization by Dilley and O'Brien (1998), with parameters optimized by Juszak and Pellicciotti (2013).

As there were no specific measurements in the Río del Yeso catchment, we adopted a value of 0.94 $Wm^{-1}K^{-1}$ for thermal effective conductivity (Brock *et al*., 2010) and a value of 0.95 for emissivity (Brock *et al*., 2010; Lejeune *et al*., 2013; Rounce and McKinney, 2014; Evatt *et al*., 2015). Reported values for the roughness length for momentum (z_0) for debris covered glaciers range between $z_0 = 0.0063$ (Khumbu Glacier, Takeuchi *et al*. 2000) and $z_0 = 0.016$ (Miage Glacier, Brock *et al*. (2010)). After a preliminary evaluation of our results and a comparison with the turbulent heat fluxes resulting from a point-scale energy balance at the location of the AWS on Piramide Glacier, we used a value of 6 mm for surface roughness.

In order to calculate G_{ratio}, it is necessary to estimate the vertical temperature profiles in the debris layer at the acquisition time of the satellite image (Equation A.3). In contrast to Rounce and McKinney (2014), we did not have buried thermistors to monitor debris temperature. As an alternative, we used the temperature profiles extracted from the point-scale surface energy balance at the location of the AWS on Piramide Glacier. This procedure allowed to follow one of the recommendations of Rounce and McKinney (2014), which is to use d_1 (Equation A.3) as thin as possible. We used d1 as the debris thickness of the first layer in the point-scale energy balance model (2 cm).

Bands 10 and 11 of LANDSAT 8 satellite images are retrieved by the Thermal Infrared Sensor and are available at a nominal resolution of 30 m (100-m real resolution). Following the procedure described in the LANDSAT 8 user manual (USGS, 2015), we converted to top of atmosphere radiance using Equation A.5 and then to

at-satellite brightness temperature using Equation A.6. We only used band 10 because band 11 was negatively affected by thermal energy from outside the field of view (i.e. stray-light) (USGS, 2015). The relevant equations are:

$$L_\lambda = ML \cdot Q_{cal} + AL, \tag{A.6}$$

where L_λ is the top of atmosphere spectral radiance [W m^{-2} srad microm], ML is Band-specific multiplicative rescaling factor from the metadata, AL is Band-specific additive rescaling factor from the metadata and Q_{cal} is quantized and calibrated standard product pixel values (DN).

$$T = \frac{K_2}{\log\left(\frac{K_1}{L_\lambda} + 1\right)}, \tag{A.7}$$

where T is at-satellite brightness temperature [K] and K_1 and K_2 are band-specific thermal conversion constants from the metadata.

All input data and the surface temperature map obtained as described in Equations A.6 to A.7 were used to solve Equation A.5 and to derive a map of debris thickness that we assume to be constant over the period of simulations.